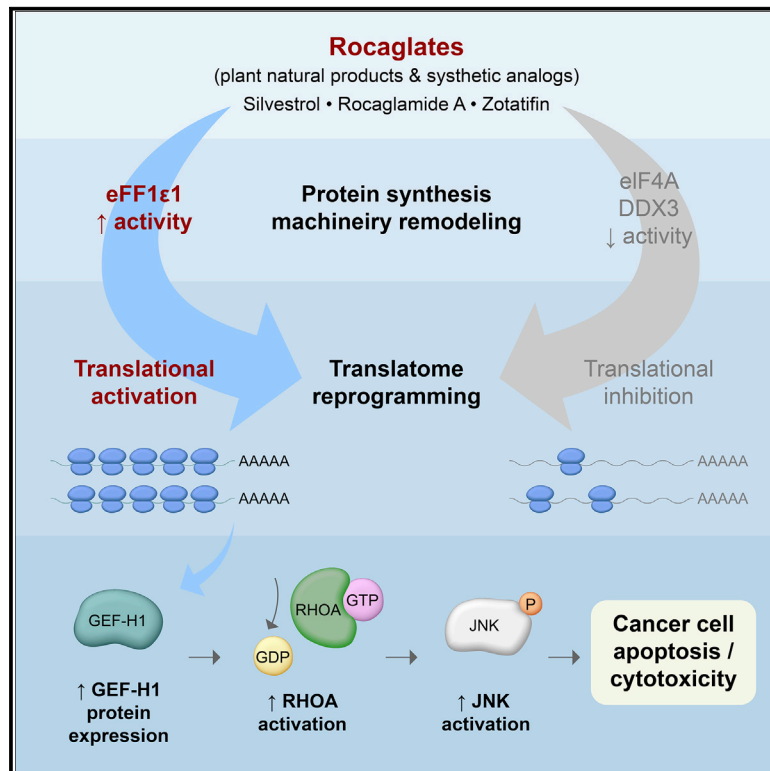**Article**

Proteomics reveal cap-dependent translation inhibitors remodel the translation machinery and translatome

Graphical abstract

Authors

J.J. David Ho, Tyler A. Cunningham, Paola Manara, ..., Jonathan R. Krieger, Stephen Lee, Jonathan H. Schatz

Correspondence

dho@hexagonbio.com (J.J.D.H.),
jschatz@med.miami.edu (J.H.S.)

In brief

Tactical protein synthesis inhibition is actively pursued as a cancer therapy that bypasses signaling redundancies limiting current strategies. Ho et al. show that rocaglates, first identified as inhibitors of eIF4A activity, globally reprogram cellular translation at both protein synthesis machinery and translatome levels, inducing cytotoxicity through anti-survival GEF-H1/RHOA/JNK signaling.

Highlights

- Rocaglates both inhibit and activate different protein synthesis factors

- Downstream translatome remodeling includes substantial translational activation

- Rocaglates induce eEF1ε1-dependent proapoptotic GEF-H1/RHOA/JNK signaling in cancer cells

- Cytotoxicity not replicated by eIF4A silencing urges re-evaluation of drug mechanisms

CellPress

Cell Reports

Article

Proteomics reveal cap-dependent translation inhibitors remodel the translation machinery and translatome

J.J. David Ho,[1,2,9,10,*] Tyler A. Cunningham,[1,3,4,9] Paola Manara,[1,5] Caroline A. Coughlin,[1,3,5] Artavazd Arumov,[1,5] Evan R. Roberts,[1,6] Ashanti Osteen,[1,6] Preet Kumar,[1,2] Daniel Bilbao,[1,6] Jonathan R. Krieger,[8] Stephen Lee,[1,7] and Jonathan H. Schatz[1,2,11,*]

[1]Sylvester Comprehensive Cancer Center, University of Miami Miller School of Medicine, Miami, FL 33136, USA
[2]Division of Hematology, Department of Medicine, University of Miami Miller School of Medicine, Miami, FL 33136, USA
[3]Medical Scientist Training Program, University of Miami Miller School of Medicine, Miami, FL 33136, USA
[4]Molecular and Cellular Pharmacology Graduate Program, University of Miami Miller School of Medicine, Miami, FL 33136, USA
[5]Sheila and David Fuente Graduate Program in Cancer Biology, University of Miami Miller School of Medicine, Miami, FL 33136, USA
[6]Cancer Modeling Shared Resource, Sylvester Comprehensive Cancer Center, University of Miami Miller School of Medicine, Miami, FL 33136, USA
[7]Department of Biochemistry and Molecular Biology, University of Miami Miller School of Medicine, Miami, FL 33136, USA
[8]Bioinformatics Solutions Inc., Waterloo, ON N2L 6J2, Canada
[9]These authors contributed equally
[10]Present address: Hexagon Bio, Menlo Park, CA 94025, USA
[11]Lead contact
*Correspondence: dho@hexagonbio.com (J.J.D.H.), jschatz@med.miami.edu (J.H.S.)
https://doi.org/10.1016/j.celrep.2021.109806

SUMMARY

Tactical disruption of protein synthesis is an attractive therapeutic strategy, with the first-in-class eIF4A-targeting compound zotatifin in clinical evaluation for cancer and COVID-19. The full cellular impact and mechanisms of these potent molecules are undefined at a proteomic level. Here, we report mass spectrometry analysis of translational reprogramming by rocaglates, cap-dependent initiation disruptors that include zotatifin. We find effects to be far more complex than simple "translational inhibition" as currently defined. Translatome analysis by TMT-pSILAC (tandem mass tag-pulse stable isotope labeling with amino acids in cell culture mass spectrometry) reveals myriad upregulated proteins that drive hitherto unrecognized cytotoxic mechanisms, including GEF-H1-mediated anti-survival RHOA/JNK activation. Surprisingly, these responses are not replicated by eIF4A silencing, indicating a broader translational adaptation than currently understood. Translation machinery analysis by MATRIX (mass spectrometry analysis of active translation factors using ribosome density fractionation and isotopic labeling experiments) identifies rocaglate-specific dependence on specific translation factors including eEF1ε1 that drive translatome remodeling. Our proteome-level interrogation reveals that the complete cellular response to these historical "translation inhibitors" is mediated by comprehensive translational landscape remodeling.

INTRODUCTION

Dynamic, global translational modifications as a rheostat of cellular adaptation represent a newer and evolving paradigm (Buszczak et al., 2014; Genuth and Barna, 2018; Ho and Lee, 2016), in contrast to traditional transcription-centric models. As the most energy-consuming cellular investment (Li et al., 2014), the complexity of eukaryotic protein synthesis machinery (Jackson et al., 2010) provides intricate, precise control over protein production during cellular state transition (Ho and Lee, 2016; Liu et al., 2016). Accumulating evidence (Cai et al., 2020; de la Parra et al., 2018; Landon et al., 2014; Lee et al., 2015; Liu et al., 2016; Schwanhäusser et al., 2011; Vogel and Marcotte,

2012), including ours (Balukoff et al., 2020; Ho et al., 2016, 2018, 2020), demonstrates the predominance of translation efficiency (TE) and translation machinery adaptations over transcript-level fluctuations in determining protein output (translatome) and phenotype in human cells responding to physiologic stimuli. In this study, we address whether this paradigm also applies to therapeutic interventions, especially those traditionally thought to elicit translational inhibition as their sole mode of action.

Activation of protein synthesis is a critical convergence for oncogenic signals (Bhat et al., 2015; Blagden and Willis, 2011; Robichaud et al., 2019; Truitt and Ruggero, 2016), and targeted manipulation of cap-dependent translation is therefore a highly
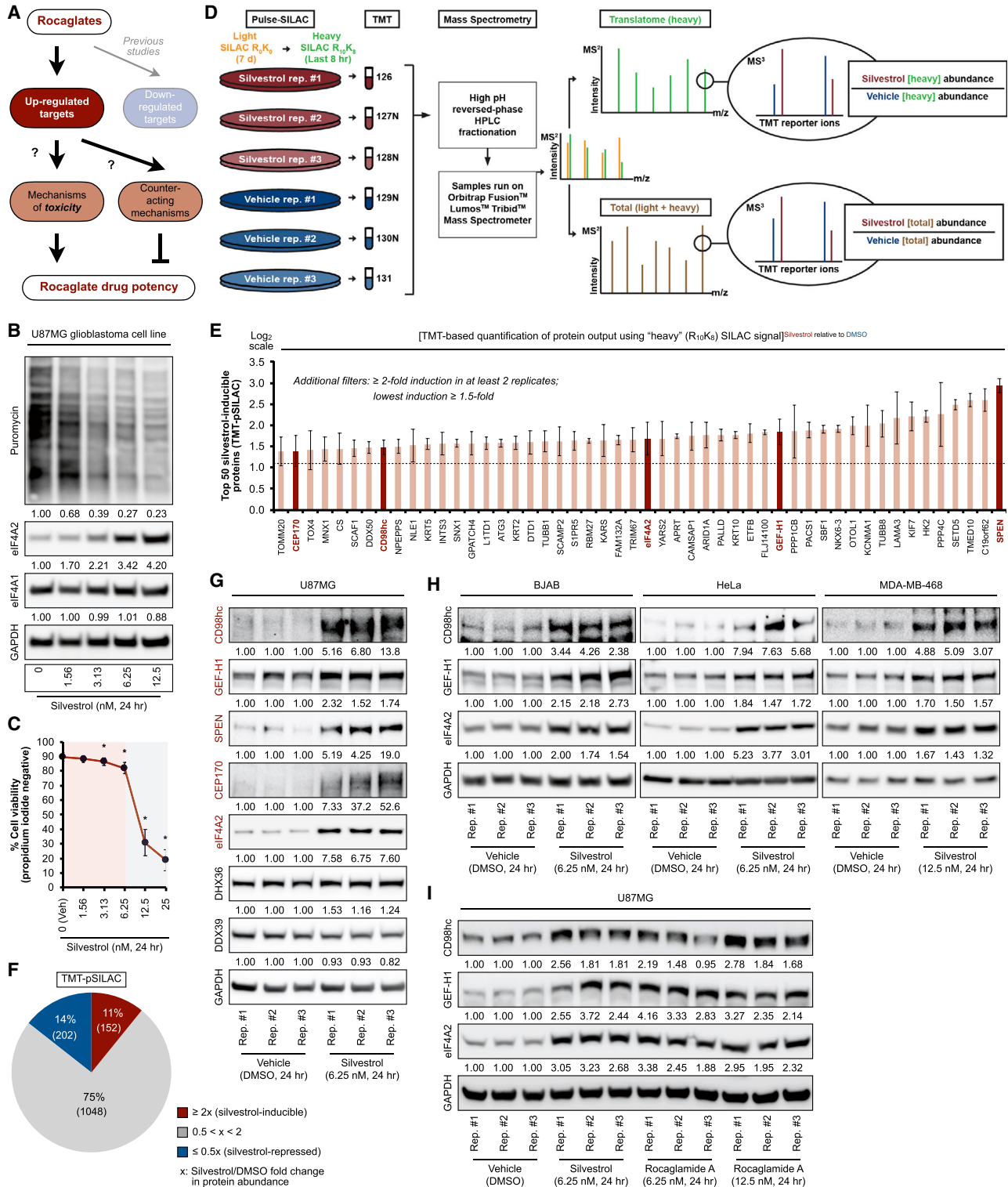
Figure 1. TMT-pSILAC reveals rocaglate-dependent translatome remodeling

(A) Schematic of this study's focus on rocaglate-inducible proteins and the functional significance.

(B) Representative immunoblots of U87MG treated with indicated concentrations of silvestrol for 24 h. Samples were loaded based on equal cell number. Densitometry values (mean of three independent experiments) are normalized to loading control. 0 nM, vehicle (DMSO).

(legend continued on next page)

attractive strategy for cancer therapy (Bhat et al., 2015; Blagden and Willis, 2011; Bruno et al., 2017; Malka-Mahieu et al., 2017; Robichaud et al., 2019; Truitt and Ruggero, 2016), as it bypasses signaling redundancies that limit the efficacy of many existing therapeutic strategies (Boussemart et al., 2014; Cerezo et al., 2018; Chan et al., 2019; Schatz et al., 2011; Wiegering et al., 2015). In particular, eIF4A1, the RNA helicase core and only enzyme of the translation initiation complex, has emerged as a leading target (Chu and Pelletier, 2015; Chu et al., 2019; Cunningham et al., 2018; Kong et al., 2019; Naineni et al., 2020). Compounds that alter eIF4A activity elicit strong potency against myriad cancers (Alachkar et al., 2013; Bordeleau et al., 2008; Cencic et al., 2013; Chan et al., 2019; Chen et al., 2019; Chu et al., 2016; Kogure et al., 2013; Lucas et al., 2009; Manier et al., 2017; Oblinger et al., 2016; Peters et al., 2018; Saradhi et al., 2011), circumventing limitations of targeting other translational mechanisms (Müller et al., 2019; Wiegering et al., 2015). In particular, rocaglates (Bordeleau et al., 2008; Novac et al., 2004) demonstrate anti-cancer potency *in vitro* and *in vivo* (Alachkar et al., 2013; Bordeleau et al., 2008; Kogure et al., 2013; Lucas et al., 2009; Manier et al., 2017; Novac et al., 2004; Saradhi et al., 2011) and are also effective against parasitic (Langlais et al., 2018), fungal (Iyer et al., 2020), and viral (Gordon et al., 2020; Müller et al., 2020; Todt et al., 2018) infections, including SARS-CoV-2 (Gordon et al., 2020; Mani et al., 2020). Zotatifin/eFT226 (Ernst et al., 2020; Thompson et al., 2021) recently became the first rocaglate to enter use in humans, entering clinical evaluation for advanced solid tumors (ClinicalTrials.gov: NCT04092673) and COVID-19 (ClinicalTrials.gov: NCT04632381). These endeavors are premised solely on the understanding of these compounds as disruptors of eIF4A activity (Chan et al., 2019; Chu et al., 2020; Gandin et al., 2016; Iwasaki et al., 2016; Iwasaki et al., 2019; Rubio et al., 2014; Thompson et al., 2021; Wolfe et al., 2014). Development of rocaglates as therapeutic agents injects urgency for a more complete understanding of their mechanisms and the biology of cellular responses beyond eIF4A inhibition. Indeed, recent work revealed that RNA helicase DDX3 is also a specific rocaglate target (Chen et al., 2021), but implications of the full spectrum of targets are unexplored. In particular, a key outstanding question is the extent to which the phenotypic effects of rocaglates are driven by inducible/upregulated proteins and preferentially engaged translation factors.

A paucity of proteomic profiling is a limiting factor in our current understanding of cellular drug responses and is only beginning to be addressed (Frejno et al., 2020; Zhao et al., 2020). Notably, Liu et al. (2017) demonstrated that drug-induced proteomic changes in cancer cells are not well captured by indirect,

RNA-based strategies alone. In this light, the field of protein synthesis inhibition has historically relied on oblique RNA-centric approaches, e.g., ribosome-bound mRNAs. Unbiased proteomic analyses of protein output or translation machinery remodeling in response to rocaglates in particular currently do not exist. The potency of these classic translation "inhibitors" across cancers raises key questions as to whether results inferred from RNA-based approaches provide a complete picture (Alachkar et al., 2013; Bordeleau et al., 2008; Cencic et al., 2009; Lucas et al., 2009; Schatz et al., 2011). In this study, we employed proteome-centric strategies to address this limitation, directly measuring protein output and adaptations in the translation machinery using tandem mass tag-pulse stable isotope labeling with amino acids in cell culture mass spectrometry (TMT-pSILAC) and our recently developed MATRIX (mass spectrometry analysis of active translation factors using ribosome density fractionation and isotopic labeling experiments) platform (Balukoff et al., 2020; Ho et al., 2018, 2020), respectively.

We find that rocaglates, including zotatifin, promote extensive remodeling of the protein synthesis machinery and translatome, unexpected based on current knowledge, thereby emphasizing the need to expand pursuit of targets and mechanisms of these drugs classically understood as one-dimensional protein synthesis inhibitors. From a broader perspective, our data highlight global translational remodeling as a key concept for cellular response to pharmacologic interventions.

RESULTS

Proteomics reveal paradoxical induction of specific proteins in response to rocaglates

To uncover the full cellular response to rocaglates, we performed proteomic interrogation of the rocaglate-dependent translatome response. Our approach fills a critical knowledge gap regarding rocaglate mechanisms mediated by induced proteins that affect cytotoxicity and clinical potency, complementing previous studies focused on downregulated targets (Figure 1A). We first established a therapeutically relevant model of rocaglate therapy using concentrations of the archetypal family member silvestrol (Schulz et al., 2021) that correspond to reported therapeutic windows (Alachkar et al., 2013; Lucas et al., 2009; Saradhi et al., 2011) over a physiologically relevant period of 24 h (Figures 1B and 1C). This contrasts with previous mechanistic studies that utilized highly concentrated doses (less therapeutically relevant) over a short period of time. Specifically, silvestrol at 6.25 nM elicited a measurable decrease in global translational intensity (Figure 1B) and proliferation (Figure S1A) without major cell death, permitting

---

(C) Percent cell viability based on propidium iodide exclusion in U87MG treated with indicated concentrations of silvestrol for 24 h. Data represent mean ± SEM (error bars) of three independent experiments. *p < 0.05 compared to vehicle. Pink-shaded area highlights concentrations at which cell viability was largely maintained (>80%).

(D) TMT-pSILAC workflow to identify silvestrol-induced (6.25 nM, 24 h) changes in protein output.

(E) Top 50 silvestrol-inducible proteins identified by TMT-pSILAC. The following criteria were applied: ≥2-fold induction in at least two replicates, with a minimum induction of ≥1.5-fold. Data represent mean ± SEM (error bars) of three independent experiments. Targets validated by immunoblot are highlighted in red.

(F) Silvestrol-induced remodeling of global protein output.

(G and H) Representative immunoblots of (G) U87MG and (H) BJAB, HeLa, and MDA-MB-468 treated with indicated concentrations of silvestrol or vehicle (DMSO) for 24 h. Silvestrol-inducible proteins are indicated in red.

(I) Representative immunoblots of U87MG treated with indicated concentrations of silvestrol, rocaglamide A, or vehicle (DMSO) for 24 h.

Densitometry values in (G), (H), and (I) are normalized to loading control. See also Figure S1.
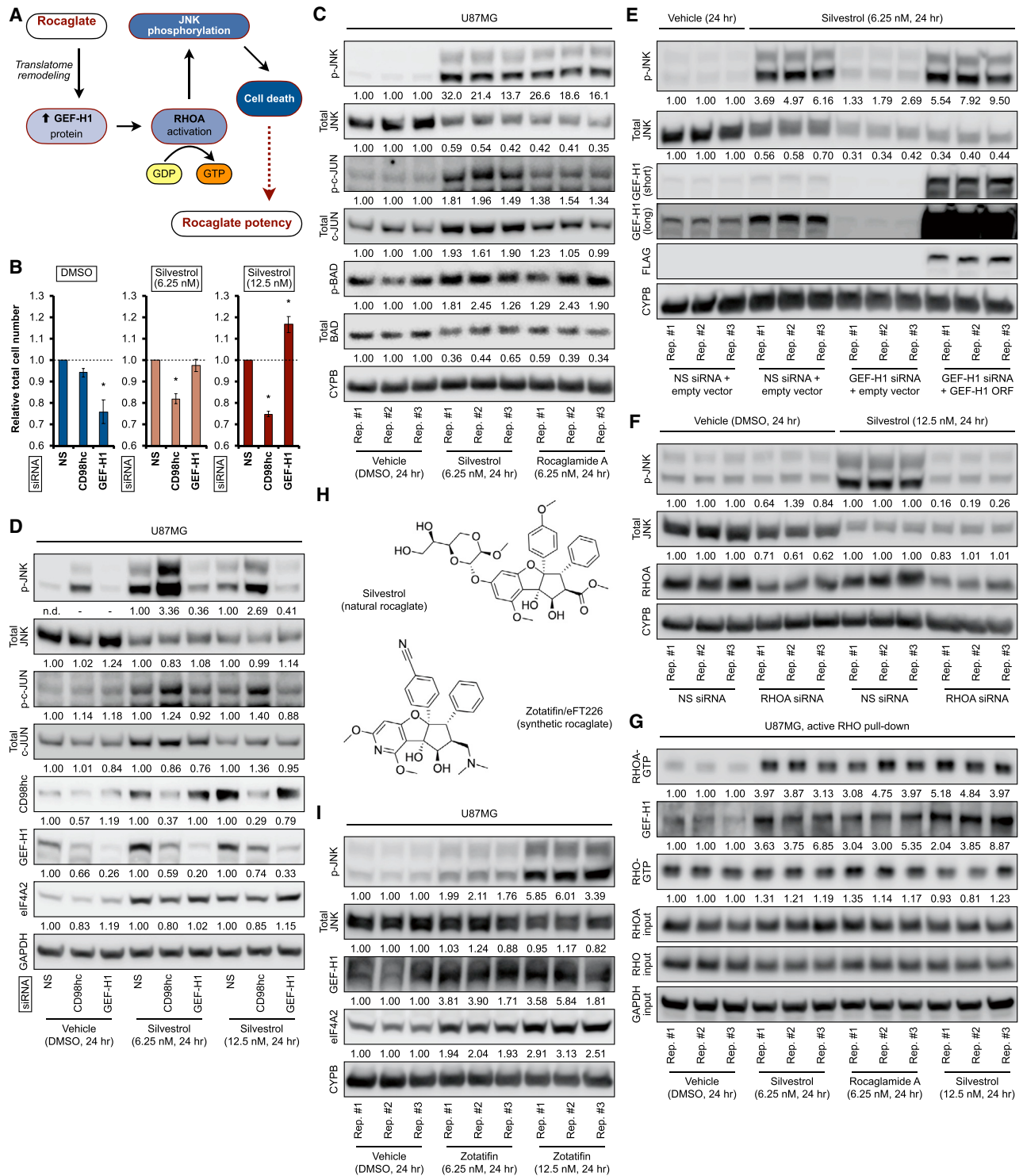
Figure 2. Rocaglate-inducible GEF-H1 regulates JNK signaling via RHOA

(A) Schematic of RHOA/JNK activation by rocaglate-induced GEF-H1 expression.

(B) Relative total cell number of U87MG treated with indicated siRNAs (pool of four independent siRNAs for each target) for 48 h, followed by silvestrol treatment at indicated concentrations or vehicle (DMSO) for 24 h. Data represent mean ± SEM (error bars) of three independent experiments. *p < 0.05 compared to NS (non-silencing) siRNA control.

(C) Representative immunoblots of U87MG treated with indicated concentrations of silvestrol, rocaglamide A, or vehicle (DMSO) for 24 h.

(legend continued on next page)

proteome interrogation from viable cells (Figure 1C). This concentration is approximately the steady-state plasma concentration of silvestrol in mice after intravenous, intraperitoneal, and oral dosing (Saradhi et al., 2011). We confirmed increased expression of eIF4A2 (Figure 1B), an established albeit poorly understood consequence of eIF4A1 loss of function (Chu et al., 2016; Galicia-Vázquez et al., 2012). We also observed changes in cell morphology, reversible upon recovery from drug withdrawal (Figure S1B), an effect reproduced by rocaglamide A (rocA), another well-characterized rocaglate (Figure S1B). We chose silvestrol (6.25 nM, 24 h) as starting conditions for subsequent experiments without confounding effects from substantial cell death. Given the robust residual intensity of global protein synthesis, we hypothesized that the emerging paradigm of adaptive, system-wide translational reprogramming operates as a key response to these compounds.

To test this hypothesis, we performed unbiased high-throughput mass spectrometry analysis of rocaglate-driven changes in protein output (translatome), using metabolic pulse-labeling (pulse-SILAC) combined with quantitative TMT labeling (TMT-pSILAC) (Figure 1D). Mass spectrometry data are deposited in the PRIDE repository and available via ProteomeXchange with identifier PXD022556 (output summarized in Table S1). We focused on those proteins (101, top 50 in Figure 1E) that exhibited $\geq$2-fold induction in at least two out of three replicates, and whose induction was at least $\geq$1.5-fold. These proteins were part of an extensive repertoire of translationally induced/upregulated proteins, comparable in number (152) to downregulated (202) counterparts (Figure 1F). Unsupervised hierarchical clustering independently confirmed upregulation of eIF4A2 (Galicia-Vázquez et al., 2012; Figure S1C), in addition to a general decrease in protein synthesis, including specific downregulated targets, e.g., PTGES3/TEBP (Iwasaki et al., 2016; Figure S1D). Consistent with changes in morphology (Figure S1B), pathway enrichment analysis revealed an over-representation of proteins involved in cytoskeletal composition and regulation, exemplified by GEF-H1, as well as cell-extracellular matrix (ECM) interactions such as CD98hc (Figure S1E). We validated by immunoblot, across several solid and blood cancer cell lines, the robust induction of multiple proteins (Figures 1G and 1H) identified by TMT-pSILAC (Figure 1E, red highlights) in response to silvestrol, which was confirmed/reproduced by rocA (Figure 1I).

Induced GEF-H1 decreases survival of rocaglate-treated cells by activating RHOA/JNK signaling

Among rocaglate-induced proteins identified by TMT-pSILAC, GEF-H1 stood out as a critical RHOA guanine nucleotide exchange factor involved in key upregulated pathways identified by enrichment analysis (Figure S1E). Given the prominent change in cell morphology and patterning consistent with RHOA activation (Figure S1B), and the recent discovery that GEF-H1 promotes JNK signaling/phosphorylation (Kashyap et al., 2019), a classic driver of apoptosis, we focused our initial efforts on GEF-H1 (Figure 2A). Transient JNK phosphorylation was noted previously in T lymphocytes and leukemia cell lines treated briefly with high (therapeutically implausible) doses of rocaglates, but biological relevance, mechanisms, and applicability across cell types were not investigated (Proksch et al., 2005; Zhu et al., 2007). We found that GEF-H1 silencing in silvestrol-treated cells increased cell number, especially at doses promoting cytotoxicity (Figures 1C and 2B). Notably, GEF-H1 depletion exerted opposite effects in rocaglate- versus vehicle-treated cells (Figure 2B). The surface antigen CD98hc/4F2 (also identified by pathway enrichment analysis) was included as a control and is addressed further in Figure S3E. In line with increased GEF-H1 expression and activity, we found that rocaglate treatment dramatically increased phosphorylation of JNK and its canonical downstream targets c-JUN and BAD (Figure 2C). Our data suggest that rocaglate-induced JNK phosphorylation is a general response across solid and blood cancer types (Figure S2A). In contrast, rocaglates did not induce GEF-H1 protein expression or JNK phosphorylation in the non-oncogenic embryonic fibroblast cell line NIH/3T3 (Figure S2B). Notably, JNK phosphorylation was attenuated by GEF-H1 silencing (Figure 2D), and rescue confirmed the role of GEF-H1 in activating JNK (Figure 2E). Specifically, endogenous GEF-H1 was silenced by 3′ UTR-targeting small interfering RNAs (siRNAs) (pool of two unique species, distinct from the siRNA pool used in Figure 2C), and GEF-H1 expression was rescued via introduction of an siRNA-insensitive, open reading frame (ORF)-only GEF-H1-FLAG construct. Results showed dramatic rescue of JNK phosphorylation by GEF-H1 re-expression (Figure 2E). Consistent with GEF-H1's established role in RHOA activation, RHOA silencing reproduced the effects of GEF-H1 knockdown, attenuating JNK phosphorylation (Figure 2F) and increasing total cell number during rocaglate treatment (Figure S2C). In addition, pull-down of active (GTP-bound) total RHO confirmed increased RHOA activation and elevated GEF-H1/RHO interactions (Figure 2G). To determine kinetics of this response, time course experiments showed initial protein induction of eIF4A2, GEH-H1, and CD98hc protein expression at 8 h of silvestrol treatment (Figure S2D). GEF-H1 translational induction at this time point was confirmed by qPCR of ribosome

(D) Representative immunoblots of U87MG treated with indicated siRNA pools for 48 h, followed by silvestrol treatment at indicated concentrations or vehicle (DMSO) for 24 h.

(E) Representative immunoblots of U87MG treated with indicated 3′ UTR-targeting siRNA pools and expression construct simultaneously for 48 h, followed by treatment with silvestrol (6.25 nM) or vehicle (DMSO) for 24 h. GEF-H1 ORF, coding region-only construct; short, short exposure; long, long exposure.
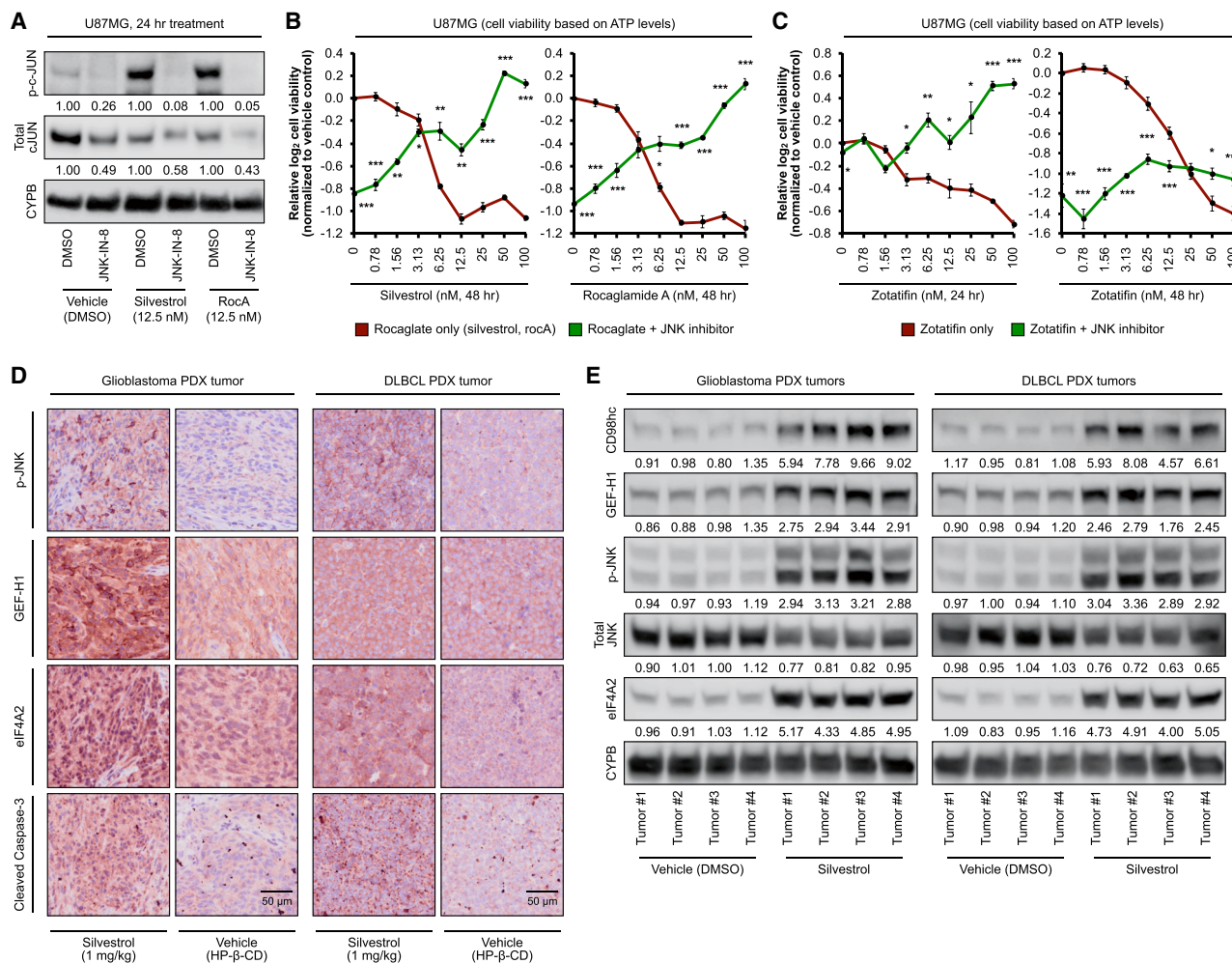
(F) Representative immunoblots of U87MG treated with indicated siRNA pools (100 nM final concentration) for 72 h, followed by treatment with silvestrol (12.5 nM) or vehicle (DMSO) for 24 h. Densitometry values in (C) and (D) are mean of three independent experiments, (E) and (F) are normalized to loading control.

(G) Representative immunoblots of active RHO (RHO-GTP) pull-down lysates from U87MG treated with indicated concentrations of silvestrol, rocaglamide A, or vehicle (DMSO) for 24 h. Densitometry values are normalized to input.

(H) Chemical structures of the natural rocaglate silvestrol and zotatifin/eFT226, a synthetic and first-in-class rocaglate to enter a clinical trial for cancer.

(I) Representative immunoblots of U87MG treated with indicated concentrations of zotatifin or vehicle (DMSO) for 24 h. Densitometry values are normalized to loading control.

See also Figure S2.

Figure 3. Rocaglate-inducible JNK phosphorylation mediates cellular toxicity signaling

(A) Representative immunoblots of U87MG treated with silvestrol (12.5 nM), rocaglamide A (rocA, 12.5 nM), or vehicle (DMSO) with and without JNK inhibitor JNK-IN-8 (10 μM) for 24 h. Densitometry values (mean of three independent experiments) are normalized to loading control.

(B and C) Relative cell viability based on ATP levels in U87MG treated with indicated concentrations of (B) silvestrol (left panel) and rocaglamide A (right panel) or (C) zotatifin with and without JNK inhibitor JNK-IN-8 (10 μM) for the indicated durations. For (B) and (C), data represent mean ± SEM (error bars) of four independent cell populations. *$p < 0.05$, **$p < 0.01$, ***$p < 0.001$ compared to corresponding rocaglate only condition.

(D) Representative immunohistochemistry images (D; scale bars represent 50 μm) and immunoblots (E) of glioblastoma (left panel) and DLBCL (right panel) patient-derived xenograft mouse tumors treated with silvestrol (1 mg/kg) or vehicle (2-hydroxypropyl-β-cyclodextrin) (daily intraperitoneal injection for 3 days). For (E), densitometry values are normalized to loading control.

See also Figure S3.

density fractions (Figure S2E). Taken together, these observations demonstrate that rocaglates translationally upregulate GEF-H1 expression to activate JNK signaling through RHOA. Next, we confirmed our findings using the clinical rocaglate zotatifin (Ernst et al., 2020; Thompson et al., 2021; Figure 2H). Similar to silvestrol and rocA, zotatifin elicited a strong increase in JNK phosphorylation, alongside increased GEF-H1 protein expression (Figure 2I). We verified the effects of zotatifin on viability to be similar to that of silvestrol (Figure S2F). These findings highlight urgent therapeutic implications of this currently uncharacterized effect of JNK-induced cytotoxicity by zotatifin, as human patients begin treatment with this compound.

From a broader perspective, the inverse correlation between JNK phosphorylation and proliferation (Figure 2) suggested an anti-survival role for JNK activation in the context of rocaglate treatment. This was confirmed with the potent JNK inhibitor JNK-IN-8 (Figure 3A), which dramatically attenuated rocaglate-induced decrease in cell viability, as demonstrated independently by measurements of ATP (Figure 3B) and cellular metabolic potential (Figure S3A). The magnitude of rescue tracked positively with increasing dosage (Figures 3B and S3A), being most prominent at rocaglate concentrations that significantly decreased cell viability (Figure 1B). We observed this rescue phenomenon also in lymphoma cells (Figure S3B). In addition, JNK inhibition
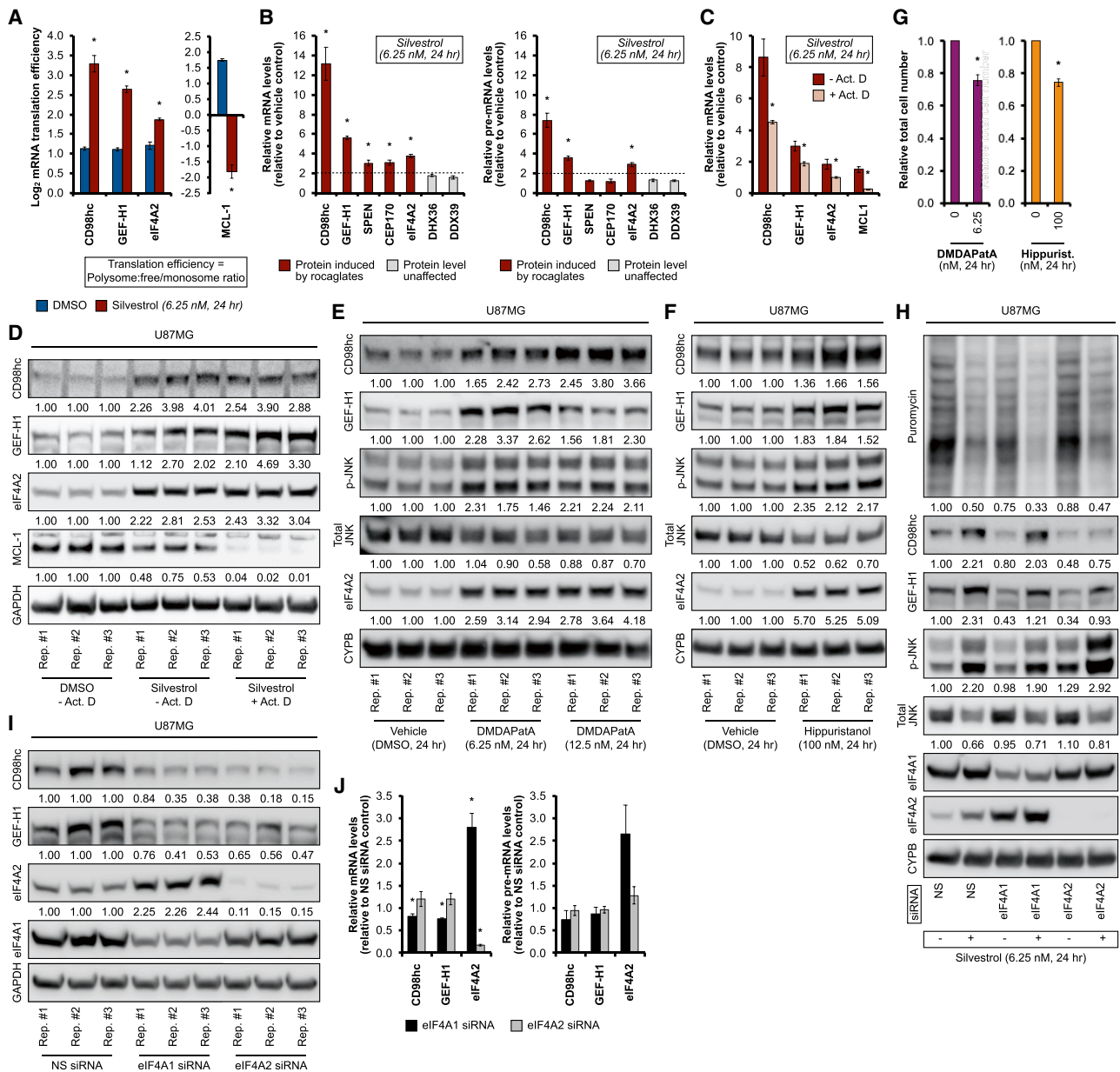
Figure 4. Mechanisms of rocaglate-dependent protein induction

(A) mRNA translation efficiency (abundance ratio of polysome-associated mRNA to ribosome-free and monosome-associated mRNA) in U87MG treated with silvestrol (6.25 nM) for 24 h. Data represent mean ± SEM (error bars) of five independent experiments. *p < 0.05 compared to vehicle (DMSO) treatment.

(B) Steady-state mature mRNA (left panel) and pre-mRNA (right panel) levels in U87MG treated with silvestrol (6.25 nM) for 24 h. Data represent mean ± SEM (error bars) of five independent experiments. *p < 0.05 compared to vehicle (DMSO) treatment. Data are normalized against 18S rRNA.

(C and D) Steady-state mRNA levels (C) and representative immunoblots (D) of U87MG treated with silvestrol (6.25 nM) for 24 h with and without actinomycin D (Act. D, 1 μg/mL, for the last 6 h of silvestrol treatment). Densitometry values in (D) are normalized to loading control. Data in (C) represent mean ± SEM (error bars) of three independent experiments. *p < 0.05 compared to no Act. D treatment.

(E and F) Representative immunoblots of U87MG treated with (E) DMDAPatA (indicated concentrations), (F) hippuristanol (100 nM), or vehicle (DMSO) for 24 h. Densitometry values in (E) and (F) are normalized to loading control.

(G) Relative total cell number of U87MG treated with DMDAPatA (6.25 nM) (left panel), hippuristanol (100 nM) (right panel), or vehicle (DMSO) for 24 h. Data represent mean ± SEM (error bars) of three independent experiments. *p < 0.05 compared to vehicle (DMSO).

(H) Representative immunoblots of U87MG treated with indicated siRNA pools for 48 h, followed by silvestrol treatment at indicated concentrations or vehicle (DMSO) for 24 h. Densitometry values (mean of three independent experiments) are normalized to loading control.

(legend continued on next page)

reproduced the effects of GEF-H1 and RHOA silencing by increasing cell number during rocaglate exposure (Figures 2A, S2B, and S3C). The anti-survival effect of JNK inhibition in rocaglate-treated cells is highlighted by the dramatic opposite effect of JNK inhibition on cell number and viability in vehicle-treated cells (Figure 3B, 3C, and S3C), as well as decreased wild-type cell numbers with GEF-H1 knockdown (Figure 2A). Apoptosis measurements further showed the rescue of rocaglate-induced cell death by JNK inhibition (Figure S3D). Further confirming the anti-survival nature of rocaglate-induced JNK activation, knockdown of CD98hc, which enhanced JNK phosphorylation (Figure 2D), further decreased cell proliferation in rocaglate-treated cells (Figure S3E). Taken together, these data support a model wherein pro-apoptotic JNK phosphorylation/signaling is activated by rocaglate-dependent GEF-H1 protein induction (Figure 2A).

Therapeutic relevance and *in vivo* confirmation of rocaglate-induced JNK activation

In line with pro-apoptotic activation of JNK signaling by the clinical rocaglate zotatifin (Figure 2H), JNK inhibition improved cellular survival in zotatifin-treated cells, highlighting therapeutic implications of our findings (Figure 3C). We verified rocaglate-dependent JNK activation *in vivo* using patient-derived xenograft (PDX) mouse tumor models, specifically a glioblastoma PDX established from a grade IV relapse tumor excised from the brain of a female patient, and a diffuse large B cell lymphoma (DLBCL) PDX established from a tumor (germinal center B cell [GCB] subtype) from the spleen of a male patient (for detailed characteristics of both models, see Table S2). Reproducing our observations in cell lines, PDX tumors treated with silvestrol (1 mg/kg) daily for 3 days exhibited robust induction of GEF-H1 protein expression and JNK phosphorylation, as demonstrated independently by immunohistochemistry (IHC) (Figures 3D and S3F) and immunoblot (Figure 3E). Measurement of apoptosis by cleaved caspase-3 further confirmed the correlation between GEF-H1 induction and increased JNK phosphorylation with tumor cell death (Figure 3D). Notably, rocaglates did not elicit such effects in healthy organs, e.g., liver and spleen (Figure S3G). In addition to GEF-H1 and JNK phosphorylation, we also confirmed increased expression of other proteins induced in response to rocaglates e.g., CD98hc and positive control eIF4A2 (Figures 3D and 3E). While our experimental design specifically assessed rocaglate-elicited changes in protein expression and post-translational modifications rather than drug efficacy, our strategy reflects published *in vivo* regimens that elicit strong anticancer activity (Alinari et al., 2012; Cerezo et al., 2018). Taken together, these results showed that GEF-H1-dependent JNK activation occurs in pathologically relevant settings *in vivo* contributing to anticancer effects of rocaglates.

Translational reprogramming mediates induction of specific proteins independently of eIF4A

Next, we wanted to determine whether induced expression of specific proteins is primarily translationally mediated. We there-

fore assessed TE through qRT-PCR analysis of the mRNA abundance ratio in polysomes (highly translated) versus ribosome-free and monosome fractions (untranslated and poorly translated). GEF-H1 and CD98hc showed a dramatic rise in TE, greater even than the previously described translational upregulation of eIF4A2 (Galicia-Vázquez et al., 2012), while MCL1 served as control as a well-established translationally downregulated rocaglate target (Figure 4A; Kogure et al., 2013; Lucas et al., 2009). Measurements of steady-state mRNA (Figure 4B, left panel) and precursor (pre-)mRNA (Figure 4B, right panel, with amplicons spanning exon-intron boundaries) indicated a transcriptional component to the upregulation of rocaglate-inducible proteins, including the previously described eIF4A2. Demonstrating predominance of translation mechanisms, however, suppression of mRNA induction (Figure 4C) with the transcriptional inhibitor actinomycin D did not attenuate protein induction (Figure 4D). Although we do not exclude contributions from protein stabilization, these findings, combined with our pSILAC analysis, which exclusively measures protein output/synthesis (Figure 1), indicated the existence of active translational mechanisms that enable the induction of these proteins in response to rocaglates in a manner independent from and predominant over mRNA-level responses.

Next, we asked whether these phenotypes are reproducible by other RNA helicase inhibitors, e.g., the pateamine A analog DMDAPatA (Chen et al., 2019; Low et al., 2005; Figure 4E) and hippuristanol (Bordeleau et al., 2006b; Novac et al., 2004; Figure 4F). Our results showed that these compounds also induced GEF-H1 and CD98hc proteins and increased JNK phosphorylation at similarly efficacious concentrations (Figure 4G). DMDA-PatA also elicited a similar morphologic change as rocaglates (Figures S4A and S4B). These results suggested eIF4A1, a common target of all of the compounds, as the driver of the observed effects, but similar to rocaglates, these RNA helicase inhibitors have additional targets (Dang et al., 2009; Lindqvist et al., 2008). Clarification of whether eIF4A1 is the primary driver fundamentally influences our basic understanding of protein synthesis, and also the mechanisms by which compounds achieve anticancer potency. Intriguingly, neither eIF4A1 nor eIF4A2 silencing affected the magnitude of rocaglate-dependent (1) GEF-H1 and CD98hc induction, (2) JNK phosphorylation, (3) decrease in overall translational intensity, or (4) change in cell morphology (Figure 4H and S4C). Furthermore, eIF4A1 or eIF4A2 depletion without rocaglate treatment (Figure 4I) failed to induce GEF-H1 and CD98hc proteins or mRNAs (Figure 4J), and it also failed to reproduce rocaglate-induced changes in morphology (Figures S4A and S4D). Since rocaglates affect both eIF4A1 and eIF4A2, we generated CRISPR-mediated eIF4A2-knockout clones in U87MG, and treated these cells with silvestrol to inhibit eIF4A1, the only other remaining eIF4A paralog targeted by rocaglates in these cells (Figure S4E). Results indicated that GEF-H1 and CD98hc protein induction was unaffected by the simultaneous inhibition of eIF4A1 and absence

---

(I and J) Representative immunoblots (I) and steady-state mRNA and pre-mRNA levels (J) of U87MG treated with indicated siRNA pools (50 nM final concentration) for 72 h. Densitometry values in (I) are normalized to loading control. Data in (J) represent mean ± SEM (error bars) of three independent experiments. *p < 0.05 compared to non-silencing (NS) siRNA control.
See also Figure S4.

of eIF4A2 (Figure S4E). This rules out eIF4A2 gain of function as a mediator of rocaglate-induced translatome remodeling and further supports a conclusion that effects are eIF4A-independent, although we do not rule out a possible difference between inhibited and absent eIF4A1 (see Discussion). Notably, additional translation inhibitors, including tunicamycin (activator of eIF2α phosphorylation-mediated integrated stress response) and 4EGI-1 (disruptor of eIF4E/eIF4G interactions) did not induce GEF-H1 or eIF4A2 proteins, unlike eIF4A-targeting compounds (Figure S4F). Weaker induction of JNK activation by these drugs suggests it is at least partly a generalized response to translational disruption, which is greatly enhanced by GEF-H1 induction in the case of the eIF4A-targeted inhibitors. Overall, these data indicate that rocaglate-driven phenotypes such as GEF-H1 protein induction and the resulting activation of anti-survival JNK signaling can be elicited by other classes of eIF4A-targeting compounds. Yet, these phenotypes represent a fundamentally different stimulus than simply reducing eIF4A expression, suggesting that effects are mediated by factors beyond eIF4A1 or eIF4A2.

Rocaglates globally reprogram the protein synthesis machinery

These results suggest drug-dependent adaptation of the protein synthesis machinery mediating translatome reprogramming. To obtain an unbiased picture, we applied our recently developed MATRIX (Balukoff et al., 2020; Ho et al., 2018, 2020) approach to silvestrol-treated cells (Figure 5A). Integrating (1) metabolic pulse labeling (pSILAC), (2) ribosome density fractionation, (3) isobaric chemical labeling using TMT for multiplexing and quantitation, and (4) mass spectrometry, MATRIX offers the capability to generate an architectural blueprint of cellular translation machineries based on protein synthesis activity. Specifically, ribosome density fractionation (Figures 5A and S5A) allows us to separate factors that are actively engaged in productive translation, i.e., polysome-associated factors, from those that are disengaged from protein synthesis, i.e., those preferentially localized to the ribosome-free ("free") fractions. Furthermore, pSILAC allows us to exclude newly synthesized peptides as a confounding signal during analysis of the factors that constitute the machinery (and not the products) of protein synthesis. Using the ratio of protein abundance in the polysome-to-ribosome-free fractions as a primary readout as previously established (Balukoff et al., 2020; Ho et al., 2018, 2020), MATRIX revealed substantial reorganization of the translation machinery, confirming downregulation of eIF4E-dependent translation (Figure 5B, blue) and an overall decrease in ribosomal engagement (Figure 5C). Alternatively, the translation elongation factor eEF1ε1, which participates in tRNA charging, demonstrated the highest increase in translational engagement out of known detected canonical translation factors (Figure 5B, red). Analysis of proteins with the highest induction in activity regardless of function (≥3-fold increase in activity) further revealed the mRNA 3′ end endonuclease CPSF73 as the most highly enriched in polysome fractions (Figure 5D, red). Given its key role in mRNA polyadenylation (Mandel et al., 2006), it is tempting to speculate that rocaglates perhaps can induce alternative polyadenylation as an additional mechanism of action, a hypothesis that remains to

be tested in future studies. Gene Ontology pathway enrichment analysis of these most highly activated proteins (Figure 5D) did not reveal any obvious or statistically significant results. Nonetheless, since eEF1ε1 is involved in tRNA charging, we analyzed relative changes in the translational activities of aminoacyl-tRNA synthetases, but none demonstrated increased polysomal engagement in response to rocaglates (Figure 5E). Given that eIF4A1/2 function as RNA helicases, we also interrogated changes in translational activities of RNA helicases, showing decreased polysome interactions of several, e.g., CNOT3 (Figure 5F, blue), and increased association of DDX17 (Figure 5F, red). The functional significance of these changes as a whole require exploration in future studies, but nonetheless they support a model that rocaglates affect translation and proteome through more than just eIF4A. As a secondary analysis of translational engagement, we also assessed the ratio of protein abundance in the polysome-to-monosome fractions (Figures S5B–S5F). A polysome-to-monosome ratio was used as a supporting rather than primary readout because the premise that monosome association reflects productive translation initiation can be confounded by various factors such as ribosome stalling, which leads to ribosome dissociation. In addition, eIF4A inhibition (by rocaglate-induced clamping) can indirectly affect translation initiation by reducing availability of functional eIF4F complexes (Chu et al., 2020; Wolfe et al., 2014). Nevertheless, both our primary and secondary analyses demonstrated increased translational activity of eEF1ε1 (Figure S5B) and CPSF73 (Figure S5D), uncovering a system-wide remodeling of the translation machinery and regulators in response to classically defined protein synthesis inhibitors. Analysis of the same mass spectrometry dataset showed that these translational adaptations were not due to changes in total protein expression (Figure S5G). Further studies are required to determine the role of other rocaglate-affected translation factors in the translatome remodeling process.

Increased eEF1ε1 activity drives rocaglate-responsive protein synthesis

As a proof of concept for rocaglate-induced translation machinery remodeling, we focused on eEF1ε1, the translation factor that exhibited the highest increase in translational activity in both primary and secondary MATRIX readouts, i.e., abundance in polysome-to-ribosome-free fractions (Figure 5B), and polysome to 40/60/80S (monosome) fractions (Figure S5B). We also examined the protein that exhibited the highest increase in polysome association overall, i.e., CPSF73 (Figures 5D and S5D). Immunoblot validation of MATRIX results confirmed increased polysome association of eEF1ε1 and CPSF73, as well as decreased engagement of eIF4E, in rocaglate-treated cells (Figure 6A). Silvestrol clamps eIF4A onto polypurine and polypyrimidine sequences on mRNA (Chu et al., 2020), resulting in increased association with mRNA templates and ribosomal stalling. This was reflected in our MATRIX analysis (Figure 5B), which we also validated by immunoblot (Figure 6A). Next, we tested functional effects of eEF1ε1 and CPSF73 on protein synthesis in cells with functional versus inhibited eIF4A. Notably, eEF1ε1 silencing specifically reduced global translational intensity (puromycin incorporation) in rocaglate-treated, but not vehicle-treated, cells (Figure 6B). In contrast
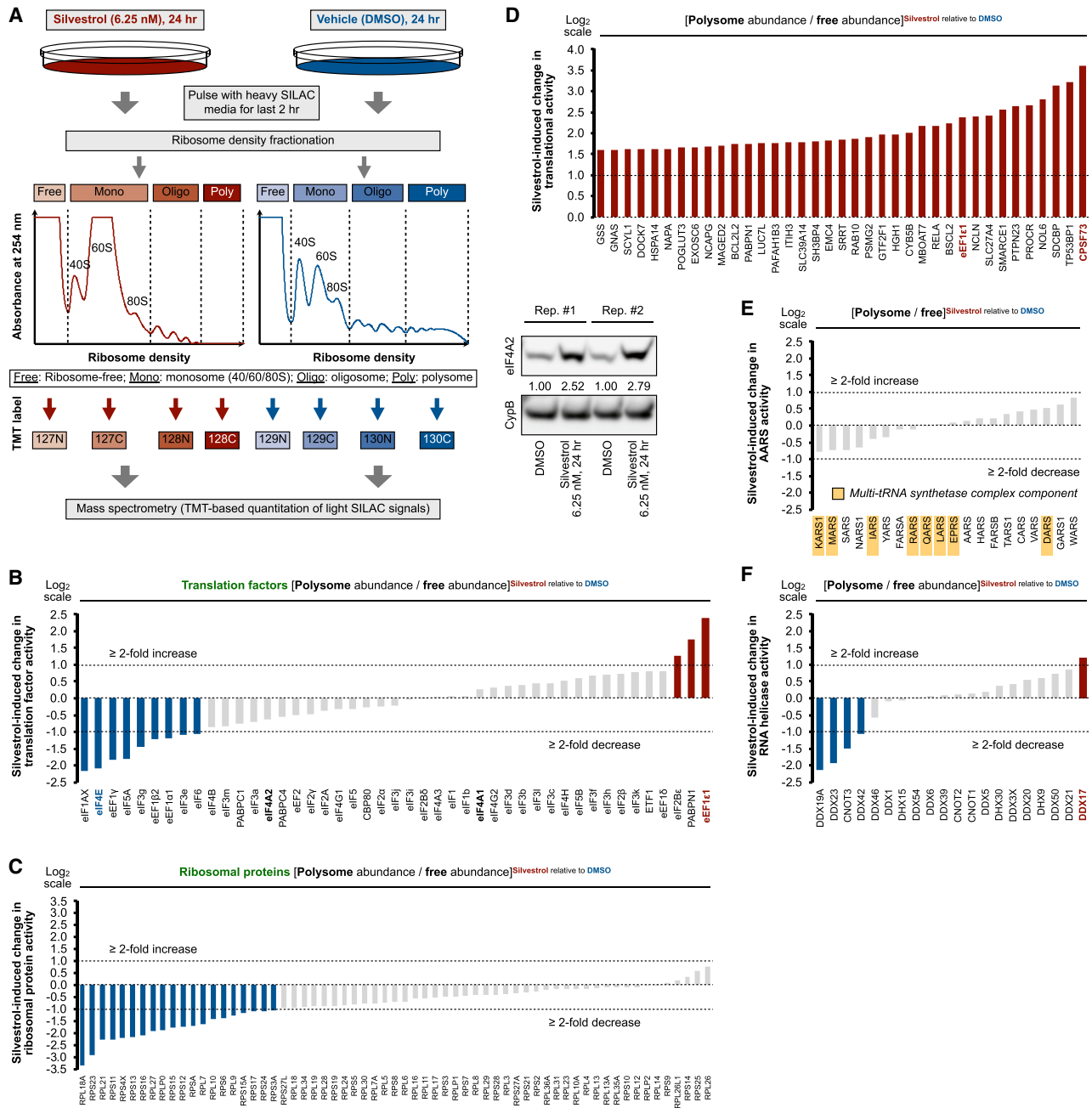
Figure 5. System-wide survey of rocaglate-dependent changes in the translation machinery

(A) MATRIX workflow of silvestrol treatment in U87MG. Polysome fractions reflect productive, high-intensity protein synthesis, whereas ribosome-free fractions are associated with translational inactivity. Representative immunoblots of U87MG input samples for ribosome density fractionation, lysed with polysome lysis buffer, are shown at the bottom right.

(B–F) MATRIX analysis of silvestrol-induced changes in translational activity (i.e., ratio of protein abundance in polysome versus ribosome-free [free] fraction) for (B) canonical translation factors, (C) ribosomal proteins, (D) most highly induced proteins (≥3-fold activity enrichment), (E) aminoacyl-tRNA synthetases (AARSs), and (F) DEAD/DEAH RNA helicases. Blue and red indicate silvestrol-repressed and silvestrol-activated translational assets (≥2-fold difference in activity), respectively.

See also Figure S5.

to eEF1ε1, CPSF73 knockdown decreased global translation regardless of treatment (Figure 6B). Given its required role in gene expression and embryonic or early lethality in knockout or knockdown organisms (Dominski et al., 2005), this result was not surprising, although it does not rule out enhanced translational activity of CPSF73 during rocaglate exposure. Indeed, consistent
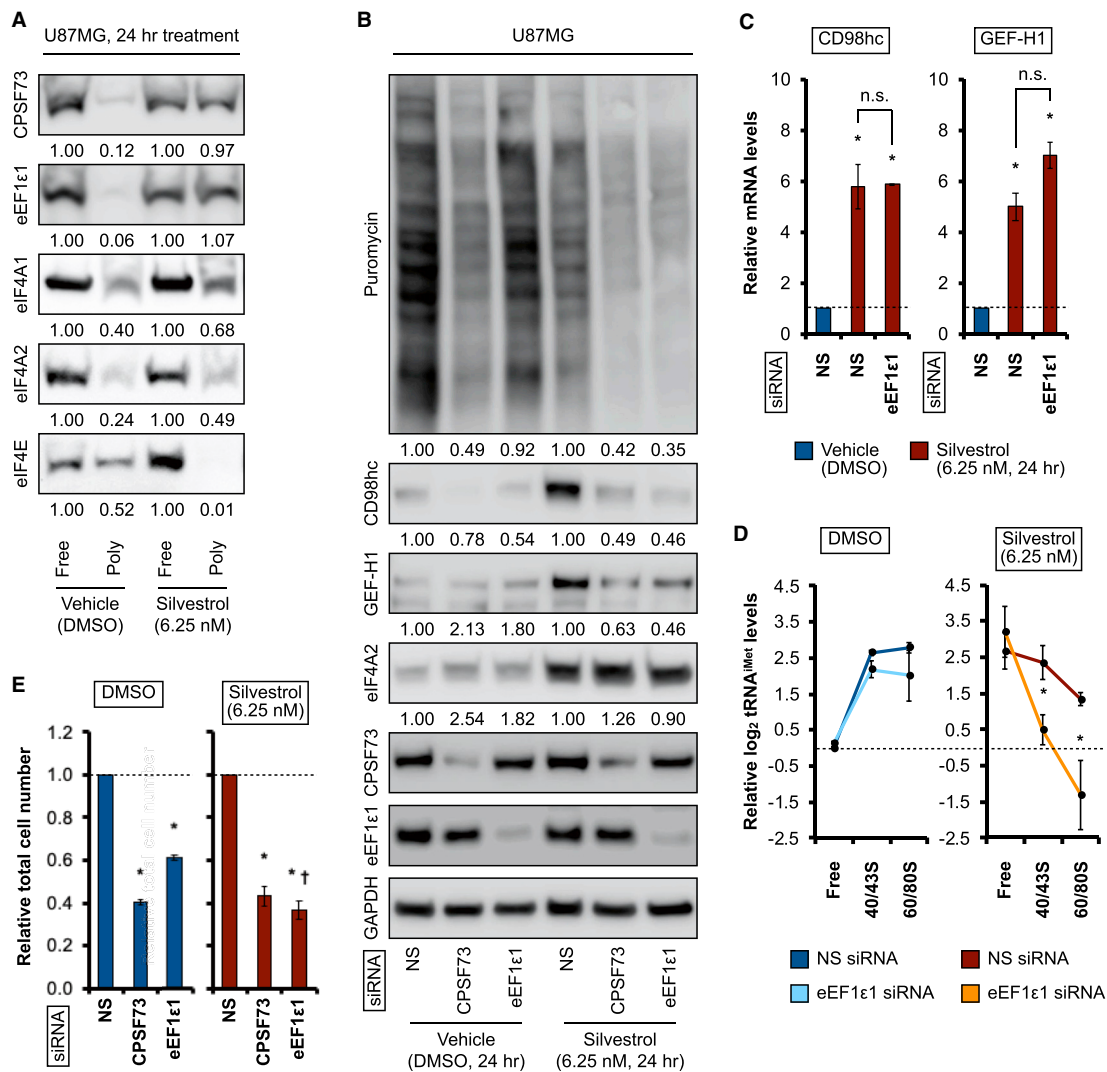
Figure 6. Increased eEF1ε1 activity enables rocaglate-driven protein synthesis

(A) Representative immunoblots of ribosome density fractions from U87MG treated with silvestrol (6.25 nM) or vehicle (DMSO) for 24 h. Free, ribosome-free fraction; Poly, polysome fraction.

(B) Representative immunoblots of U87MG treated with indicated siRNA pools for 48 h, followed by treatment with silvestrol (6.25 nM) or vehicle (DMSO) for 24 h. Densitometry values in (A) and (B) (mean of three independent experiments) are normalized to loading control.

(C) Steady-state mRNA levels of U87MG treated with indicated siRNA pools for 48 h, followed by treatment with silvestrol (6.25 nM) or vehicle (DMSO) for 24 h. Data represent mean ± SEM (error bars) of three independent experiments. *$p < 0.05$ compared to non-silencing (NS) siRNA control.

(D) Relative initiator methionine tRNA (tRNA^{iMet}) levels associated with ribosome-free fractions and translation initiation complexes (40/43S pre-initiation complex, and 60/80S monosomes) in U87MG treated with indicated siRNA pools for 48 h, followed by treatment with silvestrol (6.25 nM) or vehicle (DMSO) for 24 h and ribosome density fractionation. Data represent mean ± SEM (error bars) of three independent experiments. *$p < 0.05$ compared to corresponding fraction of non-silencing (NS) siRNA control.

(E) Relative total cell number of U87MG treated with indicated siRNA pools for 48 h, followed by silvestrol treatment at indicated concentrations or vehicle (DMSO) for 24 h. Data represent mean ± SEM (error bars) of three independent experiments. *$p < 0.05$ compared to NS siRNA control; †$p < 0.05$ compared to same target knockdown in vehicle-treated condition.

See also Figure S6.

with increased translational activity (a predominantly cytoplasmic event), we observed a rocaglate-dependent increase in both CPSF73 polysome association (Figure 6A) and cytoplasmic residency (Figure S6A). Nonetheless, eEF1ε1 knockdown specifically inhibited rocaglate-specific protein induction, e.g., GEF-H1 and CD98hc (Figure 6B), despite maintenance of robust mRNA induc-

tion (Figure 6C). Together with transcriptional inhibition experiments (Figures 4J and 4K), these findings demonstrated the predominance of translational mechanisms in upregulating roca-glate-inducible proteins. Strikingly, eIF4A2 induction was not affected by either eEF1ε1 or CPSF73 knockdown (Figure 6B). Therefore, eIF4A2 induction, activated by either rocaglates or
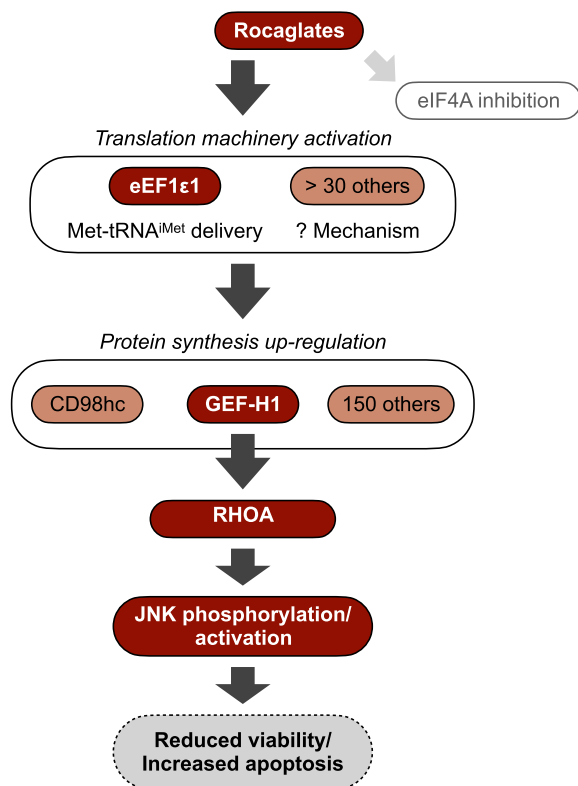
Figure 7. Model of rocaglate-specific translational remodeling
Existing studies frame rocaglates as pure eIF4A/translation inhibitors. This study conceptually redefines rocaglates as translation remodelers that reprogram both the translation machinery, e.g., increasing eEF1ε1 translational activity, as well as the translatome, including the upregulation of numerous proteins, e.g., GEF-H1, that mediate rocaglate cytotoxicity in cancer cells. As a proof of concept, GEF-H1 activates RHOA, leading to increased JNK phosphorylation and apoptotic signaling resulting in reduced cell viability.

eIF4A1 silencing (Figures 4A and 4B), is clearly mechanistically distinct from the unique translational effects of rocaglates.

Mechanistically, eEF1ε1 knockdown reduced the levels of initiator methionine tRNA (tRNA^{iMet}) associated with initiation complexes uniquely in rocaglate-treated cells, demonstrating an induced dependence on this factor (Figure 6D). Rocaglates therefore induce specific dependence on eEF1ε1's established roles in translation initiation of delivering charged initiator methionine-tRNA (met-tRNA^{iMet}) to ribosomes (Kang et al., 2012; Kwon et al., 2011), and as a scaffold protein for the macromolecular multi-tRNA synthetase complex (Han et al., 2006; Quevillon and Mirande, 1996; Quevillon et al., 1999). Further supporting the rocaglate-specific increase in its activity, eEF1ε1 knockdown led to a greater decrease in proliferation in rocaglate- versus vehicle-treated cells (Figure 6E). Taken together, these results demonstrate that rocaglates enhance eEF1ε1 translational activity to enable synthesis of specific proteins. In contrast, silencing of translation factors identified by MATRIX that either have no change in activity (e.g., eIF4A3) or decreased activity (e.g., eEF1AX) (Figure 5B) had no effect on rocaglate responses (Figure S6B). We note that eIF4A3 is traditionally considered a member of the exon junction complex, and it plays a role in the

pioneer round of translation in the nucleus, nonsense-mediated decay, and mRNA cytoplasmic export (Chan et al., 2004; Choe et al., 2014; Ryu et al., 2019). Along with earlier results (Figures 4 and S4), these findings reveal that rocaglates lead to a unique remodeling of the translation machinery and translatome. This also includes enhanced DDX17 translational activity. Specifically, DDX17 silencing confirmed MATRIX results (Figure 5F), showing attenuated induction of JNK phosphorylation, and protein levels of GEF-H1, CD98hc, and eIF4A2 (but not eIF4A1) (Figure S6C). Additional targets identified through the predefined 2-fold cutoff in translational activity (Figure 5) will require future empirical validation.

We showed here that rocaglates enhance activities and cellular dependence on specific translation factors, e.g., eEF1ε1, that drive the induction of proteins controlling the anticancer effects of these drugs, including members currently in trials (Figure 7). These findings redefine rocaglates from pure translation inhibitors to protein synthesis remodelers that rewire both the translatome and translation machinery.

DISCUSSION

The predominance of translational regulation and TE over transcript-level fluctuations occurs during evolution (Khan et al., 2013; Wang et al., 2020), development (Kronja et al., 2014), differentiation (Kristensen et al., 2013; Lu et al., 2009), circadian regulation (Huang et al., 2013), and stress adaptation (Cheng et al., 2016; Ho et al., 2016; Hsieh et al., 2012; Larsson et al., 2012; Robinson et al., 2017), among other contexts. We recently demonstrated the role of global translational remodeling in cells responding to physiological stimuli, e.g., hypoxia (Ho et al., 2016, 2018, 2020) and acidosis (Balukoff et al., 2020). Now we demonstrate that this translational paradigm is operative also during cellular responses to pharmacological interventions, especially in response to compounds traditionally understood as translation inhibitors. In contrast to the overwhelming focus on downregulated targets, proteins that are induced in response to rocaglates have not been widely examined. Our unbiased, proteomic approach revealed system-wide remodeling of translation machinery and translatome in response to rocaglates, including preferentially activated translation factors and upregulated proteins that influence drug activities, including zotatifin, which recently entered clinical trials. Our datasets serve as proteomic resources for identification of new drivers of drug efficacy and upregulated protein targets that may thwart it. This study overhauls the current unidimensional definition of rocaglates as pure eIF4A/translation inhibitors to translational remodeling agents that comprehensively rewire the protein synthesis machinery and protein output.

Our unbiased analysis revealed changes to the protein synthesis machinery in response to eIF4A inhibition, including enhanced eEF1ε1/AIMP3/p18 translational activity. While eEF1ε1 plays a key role in translation initiation by delivering met-tRNA^{iMet} to ribosomes (Kang et al., 2012; Kwon et al., 2011), it also possesses nuclear activity, including the regulation of senescence (Kim et al., 2019; Oh et al., 2010) and p53-mediated DNA damage response (Park et al., 2005). As a predominantly cytoplasmic protein, eEF1ε1 did not demonstrate increased nuclear residence in response to eIF4A inhibition. Together with increased polysome

engagement, decreased protein synthesis, and met-tRNA[iMet] delivery in eEF1ε1-depleted cells, our data support a predominantly translational role for eEF1ε1 during rocaglate exposure. We focused on eEF1ε1 as the most highly activated translation factor. The many additional MATRIX-identified proteins that increased translational engagement in response to rocaglates remain to be investigated, especially translatome remodelers e.g., RNA-binding proteins (Ho et al., 2020), that mediate preferential translational recruitment of specific mRNA populations. Notably, elevated eEF1ε1 expression has been observed in various cancers, including glioblastoma and lymphoma, the two diseases represented by PDX models used in this study. This serves as a potential explanation for the selective rocaglate sensitivity of tumors versus healthy tissues but would require extensive studies comparing tumor versus normal in individual patients treated with rocaglates to definitively answer. These determinations are best made as correlative studies during clinical assessments of zotatifin and future clinical rocaglates.

Our data demonstrate translational remodeling as a consistent response to rocaglates across solid and heme tumor cells lines and engrafted human tumors *in vivo*. The precise step-by-step mechanism leading to these changes, however, remains to be fully elucidated. DMDAPatA and hippuristanol, which have different mechanisms of eIF4A inhibition compared to rocaglates (Naineni et al., 2021; Shen and Pelletier, 2020; Steinberger et al., 2020), replicated at least some key reprogramming effects. Hippuristanol inhibits the interaction of both free and eIF4F-bound eIF4A with RNA (Bordeleau et al., 2006b), while pateamine is more similar to the rocaglates, increasing the target's interaction with RNA, making it less available to take part in the complex (Bordeleau et al., 2006a). This suggests a generalized cellular response to eIF4A1 inhibition, regardless of precise mode of action. Alternatively, drug-induced reprogramming was undiminished in eIF4A-depleted cells, and eIF4A1 loss of function through RNAi did not replicate these effects, strongly suggesting eIF4A1-independent responses. Possibilities include (1) eIF4A1-independent remodeling of the translation machinery induced by off-target consequences of rocaglates that are shared by DMDA-PatA and hippuristanol but not by 4EGI-1 or tunicamycin. We excluded eIF4A2 as driver with a CRISPR-deleted system, but a wide variety of additional mediators of reprogramming remain. Recent reports reveal, for example, that DDX3 is another RNA helicase affected by rocA (Chen et al., 2021). Pateamine A and hippuristanol are known to affect additional eIF4A paralogs (Dang et al., 2009; Lindqvist et al., 2008), and for all of these drugs unbiased proteome-wide assessment for additional targets has not been performed. (2) Remodeling is eIF4A1-dependent but not replicated by targeted knockdown. For example, inhibited eIF4A1 in a cell could promote formation of dysfunctional eIF4F complexes that would not be present in the case of knockdown. (3) A cancer-specific cellular stress response induced by the cytotoxicity of these compounds and that might apply also to additional classes of cytotoxic therapies. We observed, for example, a weaker induction of JNK activation in response to translational perturbations that did not upregulate GEF-H1, including tunicamycin, 4EGI-1, and knockdown of eIF4A3 or eIF1AX. GEF-H1 induction by rocaglates may therefore be a pro-apoptotic amplifier of a JNK-mediated stress response to

translational disruption that is initially less specific. Detailed follow-up studies are required and outside our current scope, but the fundamental nature of these questions, particularly point 3, illustrate the dearth of available information about translational responses to cancer therapies at an unbiased proteomic level. We hope our current proof-of-concept studies fuel substantial research moving forward to address these gaps in knowledge. Regardless, the fact that rocaglates remodel the cellular translation machinery beyond eIF4A and upregulate the adaptive synthesis of a sizeable protein population urges an overhaul to the current definition of these potent compounds, especially given their active development as cancer and antiviral therapies.

Beyond translation machinery components, we demonstrated as a proof of principle the activation of JNK signaling by inducible GEF-H1 protein as a previously uncharacterized mechanism of cytotoxicity by rocaglates. Alternatively, CD98hc, another rocaglate-inducible protein target, suppresses JNK activation to counteract rocaglate cytotoxicity. It is well established that JNK signaling effects are highly context-dependent, either promoting or antagonizing cell survival depending on myriad biological factors, including the activating stimulus/stress, cell type, and cellular environment (Sabapathy, 2012; Wagner and Nebreda, 2009; Weston and Davis, 2007). In the present study, we demonstrated examples of rocaglate-inducible proteins that activate cellular pathways converging on JNK signaling, with some that promote JNK-mediated apoptosis, e.g., the GEF-H1/RHOA axis, and others that promote survival via suppression of activation, e.g., CD98hc. This duality is a previously uncharacterized aspect of rocaglate toxicity, and a newer concept that influences strategies for development of combination therapies. Further studies are required to characterize potential effects of additional rocaglate-inducible proteins on JNK signaling. We confirmed here the rocaglate-dependent activation of prototypic JNK targets c-JUN and BAD. Comprehensive analysis of the myriad JNK downstream targets necessitate the use of unbiased approaches, e.g., phospho-proteomic screens, to fully elucidate additional downstream effects of JNK activation. We also note that apoptosis is well described as a consequence of rocaglate exposure to cancer cells, mediated by lost expression of MCL1 (Lucas et al., 2009) and key components of mitochondrial integrity (Gandin et al., 2016), among other mechanisms. Our data demonstrate for the first time an important role also for JNK, occurring downstream of increased GEF-H1 expression and consequent RHOA activation. Rescue from apoptosis by JNK inhibition demonstrates the mechanism's importance but does not define JNK activation as an apoptotic driver necessarily more or less potent than other previously reported mechanisms.

From a broader perspective, this study urges a fresh direction to understand the unique therapeutic advantages of compounds that affect eIF4A activity over those that target other translation factors (Boussemart et al., 2014; Cerezo et al., 2018; Chan et al., 2019; Chu et al., 2019; Cunningham et al., 2018; Schatz et al., 2011; Wiegering et al., 2015). Further interrogation of the >100 rocaglate-inducible proteins will reveal additional insight on rocaglate mechanisms and accelerate discovery of rational new synergy targets for combination with these agents redefined as translation-reprogramming compounds in this study.

STAR★METHODS

Detailed methods are provided in the online version of this paper and include the following:

- KEY RESOURCES TABLE
- RESOURCE AVAILABILITY
  - Lead contact
  - Materials availability
  - Data availability
- EXPERIMENTAL MODEL AND SUBJECT DETAILS
  - Cell culture and reagents
  - Mice
  - Patient-derived xenograft (PDX) tumors
- METHOD DETAILS
  - Pulse SILAC (pSILAC)
  - Ribosome density profiling
  - TMT-pSILAC mass spectrometry
  - MATRIX mass spectrometry
  - RNA interference
  - Active RHO pull-down
  - Subcellular fractionation
  - Gene Ontology (GO) pathway enrichment
  - Cell viability and apoptosis
  - Immunohistochemistry
  - Protein extraction from mouse tumors
  - Immunoblot
  - qRT-PCR
  - Primer sequences
  - CRISPR-Cas9
- QUANTIFICATION AND STATISTICAL ANALYSES

SUPPLEMENTAL INFORMATION

Supplemental information can be found online at https://doi.org/10.1016/j.celrep.2021.109806.

AUTHOR CONTRIBUTIONS

J.J.D.H. and J.H.S. conceived the study. J.J.D.H., T.A.C., and J.H.S. designed the experiments. J.J.D.H., T.A.C., P.M., C.A.C., A.A., E.R.R., A.O., P.K., D.B., and J.R.K. conducted the experiments. J.J.D.H., T.A.C., D.B., J.R.K., S.L., and J.H.S. analyzed the data. J.J.D.H. and J.H.S. wrote the manuscript, with input from all authors.

DECLARATION OF INTERESTS

The authors declare no competing interests.

REFERENCES

Alachkar, H., Santhanam, R., Harb, J.G., Lucas, D.M., Oaks, J.J., Hickey, C.J., Pan, L., Kinghorn, A.D., Caligiuri, M.A., Perrotti, D., et al. (2013). Silvestrol exhibits significant in vivo and in vitro antileukemic activities and inhibits FLT3 and *miR-155* expressions in acute myeloid leukemia. J. Hematol. Oncol. *6*, 21.

Alinari, L., Prince, C.J., Edwards, R.B., Towns, W.H., Mani, R., Lehman, A., Zhang, X., Jarjoura, D., Pan, L., Kinghorn, A.D., et al. (2012). Dual targeting of the cyclin/Rb/E2F and mitochondrial pathways in mantle cell lymphoma with the translation inhibitor silvestrol. Clin. Cancer Res. *18*, 4600–4611.

Balukoff, N.C., Ho, J.J.D., Theodoridis, P.R., Wang, M., Bokros, M., Llanio, L.M., Krieger, J.R., Schatz, J.H., and Lee, S. (2020). A translational program that suppresses metabolism to shield the genome. Nat. Commun. *11*, 5755.

Bhat, M., Robichaud, N., Hulea, L., Sonenberg, N., Pelletier, J., and Topisirovic, I. (2015). Targeting the translation machinery in cancer. Nat. Rev. Drug Discov. *14*, 261–278.

Blagden, S.P., and Willis, A.E. (2011). The biological and therapeutic relevance of mRNA translation in cancer. Nat. Rev. Clin. Oncol. *8*, 280–291.

Bordeleau, M.E., Cencic, R., Lindqvist, L., Oberer, M., Northcote, P., Wagner, G., and Pelletier, J. (2006a). RNA-mediated sequestration of the RNA helicase eIF4A by Pateamine A inhibits translation initiation. Chem. Biol. *13*, 1287–1295.

Bordeleau, M.E., Mori, A., Oberer, M., Lindqvist, L., Chard, L.S., Higa, T., Belsham, G.J., Wagner, G., Tanaka, J., and Pelletier, J. (2006b). Functional characterization of IRESes by an inhibitor of the RNA helicase eIF4A. Nat. Chem. Biol. *2*, 213–220.

Bordeleau, M.E., Robert, F., Gerard, B., Lindqvist, L., Chen, S.M., Wendel, H.G., Brem, B., Greger, H., Lowe, S.W., Porco, J.A., Jr., and Pelletier, J. (2008). Therapeutic suppression of translation initiation modulates chemosensitivity in a mouse lymphoma model. J. Clin. Invest. *118*, 2651–2660.

Boussemart, L., Malka-Mahieu, H., Girault, I., Allard, D., Hemmingsson, O., Tomasic, G., Thomas, M., Basmadjian, C., Ribeiro, N., Thuaud, F., et al. (2014). eIF4F is a nexus of resistance to anti-BRAF and anti-MEK cancer therapies. Nature *513*, 105–109.

Bruno, P.M., Liu, Y., Park, G.Y., Murai, J., Koch, C.E., Eisen, T.J., Pritchard, J.R., Pommier, Y., Lippard, S.J., and Hemann, M.T. (2017). A subset of platinum-containing chemotherapeutic agents kills cells by inducing ribosome biogenesis stress. Nat. Med. *23*, 461–471.

Buszczak, M., Signer, R.A., and Morrison, S.J. (2014). Cellular differences in protein synthesis regulate tissue homeostasis. Cell *159*, 242–251.

Cai, E.Y., Kufeld, M.N., Schuster, S., Arora, S., Larkin, M., Germanos, A.A., Hsieh, A.C., and Beronja, S. (2020). Selective translation of cell fate regulators mediates tolerance to broad oncogenic stress. Cell Stem Cell *27*, 270–283.e7.

Cencic, R., Carrier, M., Galicia-Vázquez, G., Bordeleau, M.E., Sukarieh, R., Bourdeau, A., Brem, B., Teodoro, J.G., Greger, H., Tremblay, M.L., et al. (2009). Antitumor activity and mechanism of action of the cyclopenta[*b*]benzofuran, silvestrol. PLoS ONE *4*, e5223.

Cencic, R., Robert, F., Galicia-Vázquez, G., Malina, A., Ravindar, K., Somaiah, R., Pierre, P., Tanaka, J., Deslongchamps, P., and Pelletier, J. (2013). Modifying chemotherapy response by targeted inhibition of eukaryotic initiation factor 4A. Blood Cancer J. *3*, e128.

Cerezo, M., Guemiri, R., Druillennec, S., Girault, I., Malka-Mahieu, H., Shen, S., Allard, D., Martineau, S., Welsch, C., Agoussi, S., et al. (2018). Translational control of tumor immune escape via the eIF4F-STAT1-PD-L1 axis in melanoma. Nat. Med. *24*, 1877–1886.

Chan, C.C., Dostie, J., Diem, M.D., Feng, W., Mann, M., Rappsilber, J., and Dreyfuss, G. (2004). eIF4A3 is a novel component of the exon junction complex. RNA *10*, 200–209.

Chan, K., Robert, F., Oertlin, C., Kapeller-Libermann, D., Avizonis, D., Gutierrez, J., Handly-Santana, A., Doubrovin, M., Park, J., Schoepfer, C., et al. (2019). eIF4A supports an oncogenic translation program in pancreatic ductal adenocarcinoma. Nat. Commun. 10, 5151.

Chen, R., Zhu, M., Chaudhari, R.R., Robles, O., Chen, Y., Skillern, W., Qin, Q., Wierda, W.G., Zhang, S., Hull, K.G., et al. (2019). Creating novel translation inhibitors to target pro-survival proteins in chronic lymphocytic leukemia. Leukemia 33, 1663–1674.

Chen, M., Asanuma, M., Takahashi, M., Shichino, Y., Mito, M., Fujiwara, K., Saito, H., Floor, S.N., Ingolia, N.T., Sodeoka, M., et al. (2021). Dual targeting of DDX3 and eIF4A by the translation inhibitor rocaglamide A. Cell Chem. Biol. 28, 475–486.e8.

Cheng, Z., Teo, G., Krueger, S., Rock, T.M., Koh, H.W., Choi, H., and Vogel, C. (2016). Differential dynamics of the mammalian mRNA and protein expression response to misfolding stress. Mol. Syst. Biol. 12, 855.

Choe, J., Ryu, I., Park, O.H., Park, J., Cho, H., Yoo, J.S., Chi, S.W., Kim, M.K., Song, H.K., and Kim, Y.K. (2014). eIF4AIII enhances translation of nuclear cap-binding complex-bound mRNAs by promoting disruption of secondary structures in 5′UTR. Proc. Natl. Acad. Sci. USA 111, E4577–E4586.

Chu, J., and Pelletier, J. (2015). Targeting the eIF4A RNA helicase as an anti-neoplastic approach. Biochim. Biophys. Acta 1849, 781–791.

Chu, J., Galicia-Vázquez, G., Cencic, R., Mills, J.R., Katigbak, A., Porco, J.A., Jr., and Pelletier, J. (2016). CRISPR-mediated drug-target validation reveals selective pharmacological inhibition of the RNA helicase, eIF4A. Cell Rep. 15, 2340–2347.

Chu, J., Zhang, W., Cencic, R., Devine, W.G., Beglov, D., Henkel, T., Brown, L.E., Vajda, S., Porco, J.A., Jr., and Pelletier, J. (2019). Amidino-rocaglates: A potent class of eIF4A inhibitors. Cell. Chem. Biol. 26, 1586–1593.e3.

Chu, J., Zhang, W., Cencic, R., O'Connor, P.B.F., Robert, F., Devine, W.G., Selznick, A., Henkel, T., Merrick, W.C., Brown, L.E., et al. (2020). Rocaglates induce gain-of-function alterations to eIF4A and eIF4F. Cell Rep. 30, 2481–2488.e5.

Cunningham, T.A., Chapman, E., and Schatz, J.H. (2018). eIF4A inhibition: Ready for primetime? Oncotarget 9, 35515–35516.

Dang, Y., Low, W.K., Xu, J., Gehring, N.H., Dietz, H.C., Romo, D., and Liu, J.O. (2009). Inhibition of nonsense-mediated mRNA decay by the natural product pateamine A through eukaryotic initiation factor 4AIII. J. Biol. Chem. 284, 23613–23621.

de la Parra, C., Ernlund, A., Alard, A., Ruggles, K., Ueberheide, B., and Schneider, R.J. (2018). A widespread alternate form of cap-dependent mRNA translation initiation. Nat. Commun. 9, 3068.

Dominski, Z., Yang, X.C., Purdy, M., Wagner, E.J., and Marzluff, W.F. (2005). A CPSF-73 homologue is required for cell cycle progression but not cell growth and interacts with a protein having features of CPSF-100. Mol. Cell. Biol. 25, 1489–1500.

Ernst, J.T., Thompson, P.A., Nilewski, C., Sprengeler, P.A., Sperry, S., Packard, G., Michels, T., Xiang, A., Tran, C., Wegerski, C.J., et al. (2020). Design of development candidate eFT226, a first in class inhibitor of eukaryotic initiation factor 4A RNA helicase. J. Med. Chem. 63, 5879–5955.

Frejno, M., Meng, C., Ruprecht, B., Oellerich, T., Scheich, S., Kleigrewe, K., Drecoll, E., Samaras, P., Hogrebe, A., Helm, D., et al. (2020). Proteome activity landscapes of tumor cell lines determine drug responses. Nat. Commun. 11, 3639.

Galicia-Vázquez, G., Cencic, R., Robert, F., Agenor, A.Q., and Pelletier, J. (2012). A cellular response linking eIF4AI activity to eIF4AII transcription. RNA 18, 1373–1384.

Gandin, V., Masvidal, L., Hulea, L., Gravel, S.P., Cargnello, M., McLaughlan, S., Cai, Y., Balanathan, P., Morita, M., Rajakumar, A., et al. (2016). nanoCAGE reveals 5′ UTR features that define specific modes of translation of functionally related MTOR-sensitive mRNAs. Genome Res. 26, 636–648.

Genuth, N.R., and Barna, M. (2018). Heterogeneity and specialized functions of translation machinery: From genes to organisms. Nat. Rev. Genet. 19, 431–452.

Gordon, D.E., Jang, G.M., Bouhaddou, M., Xu, J., Obernier, K., White, K.M., O'Meara, M.J., Rezelj, V.V., Guo, J.Z., Swaney, D.L., et al. (2020). A SARS-CoV-2 protein interaction map reveals targets for drug repurposing. Nature 583, 459–468.

Han, J.M., Lee, M.J., Park, S.G., Lee, S.H., Razin, E., Choi, E.C., and Kim, S. (2006). Hierarchical network between the components of the multi-tRNA synthetase complex: Implications for complex formation. J. Biol. Chem. 281, 38663–38667.

Ho, J.J.D., and Lee, S. (2016). A cap for every occasion: Alternative eIF4F complexes. Trends Biochem. Sci. 41, 821–823.

Ho, J.J.D., Wang, M., Audas, T.E., Kwon, D., Carlsson, S.K., Timpano, S., Evagelou, S.L., Brothers, S., Gonzalgo, M.L., Krieger, J.R., et al. (2016). Systemic reprogramming of translation efficiencies on oxygen stimulus. Cell Rep. 14, 1293–1300.

Ho, J.J.D., Balukoff, N.C., Cervantes, G., Malcolm, P.D., Krieger, J.R., and Lee, S. (2018). Oxygen-sensitive remodeling of central carbon metabolism by archaic eIF5B. Cell Rep. 22, 17–26.

Ho, J.J.D., Balukoff, N.C., Theodoridis, P.R., Wang, M., Krieger, J.R., Schatz, J.H., and Lee, S. (2020). A network of RNA-binding proteins controls translation efficiency to activate anaerobic metabolism. Nat. Commun. 11, 2677.

Hsieh, A.C., Liu, Y., Edlind, M.P., Ingolia, N.T., Janes, M.R., Sher, A., Shi, E.Y., Stumpf, C.R., Christensen, C., Bonham, M.J., et al. (2012). The translational landscape of mTOR signalling steers cancer initiation and metastasis. Nature 485, 55–61.

Huang, Y., Ainsley, J.A., Reijmers, L.G., and Jackson, F.R. (2013). Translational profiling of clock cells reveals circadianly synchronized protein synthesis. PLoS Biol. 11, e1001703.

Iwasaki, S., Floor, S.N., and Ingolia, N.T. (2016). Rocaglates convert DEAD-box protein eIF4A into a sequence-selective translational repressor. Nature 534, 558–561.

Iwasaki, S., Iwasaki, W., Takahashi, M., Sakamoto, A., Watanabe, C., Shichino, Y., Floor, S.N., Fujiwara, K., Mito, M., Dodo, K., et al. (2019). The translation inhibitor rocaglamide targets a bimolecular cavity between eIF4A and polypurine RNA. Mol. Cell 73, 738–748.e9.

Iyer, K.R., Whitesell, L., Porco, J.A., Jr., Henkel, T., Brown, L.E., Robbins, N., and Cowen, L.E. (2020). Translation inhibition by rocaglates activates a species-specific cell death program in the emerging fungal pathogen Candida auris. MBio 11, e03329-19.

Jackson, R.J., Hellen, C.U., and Pestova, T.V. (2010). The mechanism of eukaryotic translation initiation and principles of its regulation. Nat. Rev. Mol. Cell Biol. 11, 113–127.

Kang, T., Kwon, N.H., Lee, J.Y., Park, M.C., Kang, E., Kim, H.H., Kang, T.J., and Kim, S. (2012). AIMP3/p18 controls translational initiation by mediating the delivery of charged initiator tRNA to initiation complex. J. Mol. Biol. 423, 475–481.

Kashyap, A.S., Fernandez-Rodriguez, L., Zhao, Y., Monaco, G., Trefny, M.P., Yoshida, N., Martin, K., Sharma, A., Olieric, N., Shah, P., et al. (2019). GEF-H1 signaling upon microtubule destabilization is required for dendritic cell activation and specific anti-tumor responses. Cell Rep. 28, 3367–3380.e8.

Khan, Z., Ford, M.J., Cusanovich, D.A., Mitrano, A., Pritchard, J.K., and Gilad, Y. (2013). Primate transcript and protein expression levels evolve under compensatory selection pressures. Science 342, 1100–1104.

Kim, C., Park, J.M., Song, Y., Kim, S., and Moon, J. (2019). HIF1α-mediated AIMP3 suppression delays stem cell aging via the induction of autophagy. Aging Cell 18, e12909.

Kogure, T., Kinghorn, A.D., Yan, I., Bolon, B., Lucas, D.M., Grever, M.R., and Patel, T. (2013). Therapeutic potential of the translation inhibitor silvestrol in hepatocellular cancer. PLoS ONE 8, e76136.

Kong, T., Xue, Y., Cencic, R., Zhu, X., Monast, A., Fu, Z., Pilon, V., Sangwan, V., Guiot, M.C., Foulkes, W.D., et al. (2019). eif4a inhibitors suppress cell-cycle feedback response and acquired resistance to CDK4/6 inhibition in cancer. Mol. Cancer Ther. 18, 2158–2170.

Kristensen, A.R., Gsponer, J., and Foster, L.J. (2013). Protein synthesis rate is the predominant regulator of protein expression during differentiation. Mol. Syst. Biol. *9*, 689.

Kronja, I., Yuan, B., Eichhorn, S.W., Dzeyk, K., Krijgsveld, J., Bartel, D.P., and Orr-Weaver, T.L. (2014). Widespread changes in the posttranscriptional landscape at the *Drosophila* oocyte-to-embryo transition. Cell Rep. *7*, 1495–1508.

Kwon, N.H., Kang, T., Lee, J.Y., Kim, H.H., Kim, H.R., Hong, J., Oh, Y.S., Han, J.M., Ku, M.J., Lee, S.Y., and Kim, S. (2011). Dual role of methionyl-tRNA synthetase in the regulation of translation and tumor suppressor activity of aminoacyl-tRNA synthetase-interacting multifunctional protein-3. Proc. Natl. Acad. Sci. USA *108*, 19635–19640.

Landon, A.L., Muniandy, P.A., Shetty, A.C., Lehrmann, E., Volpon, L., Houng, S., Zhang, Y., Dai, B., Peroutka, R., Mazan-Mamczarz, K., et al. (2014). MNKs act as a regulatory switch for eIF4E1 and eIF4E3 driven mRNA translation in DLBCL. Nat. Commun. *5*, 5413.

Langlais, D., Cencic, R., Moradin, N., Kennedy, J.M., Ayi, K., Brown, L.E., Crandall, I., Tarry, M.J., Schmeing, M., Kain, K.C., et al. (2018). Rocaglates as dual-targeting agents for experimental cerebral malaria. Proc. Natl. Acad. Sci. USA *115*, E2366–E2375.

Larsson, O., Morita, M., Topisirovic, I., Alain, T., Blouin, M.J., Pollak, M., and Sonenberg, N. (2012). Distinct perturbation of the translatome by the antidiabetic drug metformin. Proc. Natl. Acad. Sci. USA *109*, 8977–8982.

Lee, A.S., Kranzusch, P.J., and Cate, J.H. (2015). eIF3 targets cell-proliferation messenger RNAs for translational activation or repression. Nature *522*, 111–114.

Li, G.W., Burkhardt, D., Gross, C., and Weissman, J.S. (2014). Quantifying absolute protein synthesis rates reveals principles underlying allocation of cellular resources. Cell *157*, 624–635.

Lindqvist, L., Oberer, M., Reibarkh, M., Cencic, R., Bordeleau, M.E., Vogt, E., Marintchev, A., Tanaka, J., Fagotto, F., Altmann, M., et al. (2008). Selective pharmacological targeting of a DEAD box RNA helicase. PLoS ONE *3*, e1583.

Liu, Y., Beyer, A., and Aebersold, R. (2016). On the dependency of cellular protein levels on mRNA abundance. Cell *165*, 535–550.

Liu, T.Y., Huang, H.H., Wheeler, D., Xu, Y., Wells, J.A., Song, Y.S., and Wiita, A.P. (2017). Time-resolved proteomics extends ribosome profiling-based measurements of protein synthesis dynamics. Cell Syst. *4*, 636–644.e9.

Low, W.K., Dang, Y., Schneider-Poetsch, T., Shi, Z., Choi, N.S., Merrick, W.C., Romo, D., and Liu, J.O. (2005). Inhibition of eukaryotic translation initiation by the marine natural product pateamine A. Mol. Cell *20*, 709–722.

Lu, R., Markowetz, F., Unwin, R.D., Leek, J.T., Airoldi, E.M., MacArthur, B.D., Lachmann, A., Rozov, R., Ma'ayan, A., Boyer, L.A., et al. (2009). Systems-level dynamic analyses of fate change in murine embryonic stem cells. Nature *462*, 358–362.

Lucas, D.M., Edwards, R.B., Lozanski, G., West, D.A., Shin, J.D., Vargo, M.A., Davis, M.E., Rozewski, D.M., Johnson, A.J., Su, B.N., et al. (2009). The novel plant-derived agent silvestrol has B-cell selective activity in chronic lymphocytic leukemia and acute lymphoblastic leukemia in vitro and in vivo. Blood *113*, 4656–4666.

Malka-Mahieu, H., Newman, M., Désaubry, L., Robert, C., and Vagner, S. (2017). Molecular pathways: The eIF4F translation initiation complex-new opportunities for cancer treatment. Clin. Cancer Res. *23*, 21–25.

Mandel, C.R., Kaneko, S., Zhang, H., Gebauer, D., Vethantham, V., Manley, J.L., and Tong, L. (2006). Polyadenylation factor CPSF-73 is the pre-mRNA 3′-end-processing endonuclease. Nature *444*, 953–956.

Mani, J.S., Johnson, J.B., Steel, J.C., Broszczak, D.A., Neilsen, P.M., Walsh, K.B., and Naiker, M. (2020). Natural product-derived phytochemicals as potential agents against coronaviruses: A review. Virus Res. *284*, 197989.

Manier, S., Huynh, D., Shen, Y.J., Zhou, J., Yusufzai, T., Salem, K.Z., Ebright, R.Y., Shi, J., Park, J., Glavey, S.V., et al. (2017). Inhibiting the oncogenic translation program is an effective therapeutic strategy in multiple myeloma. Sci. Transl. Med. *9*, eaal2668.

Müller, D., Shin, S., Goullet de Rugy, T., Samain, R., Baer, R., Strehaiano, M., Masvidal-Sanz, L., Guillermet-Guibert, J., Jean, C., Tsukumo, Y., et al. (2019). eIF4A inhibition circumvents uncontrolled DNA replication mediated by 4E-BP1 loss in pancreatic cancer. JCI Insight *4*, 121951.

Müller, C., Obermann, W., Schulte, F.W., Lange-Grünweller, K., Oestereich, L., Elgner, F., Glitscher, M., Hildt, E., Singh, K., Wendel, H.G., et al. (2020). Comparison of broad-spectrum antiviral activities of the synthetic rocaglate CR-31-B (−) and the eIF4A-inhibitor Silvestrol. Antiviral Res. *175*, 104706.

Naineni, S.K., Itoua Maïga, R., Cencic, R., Putnam, A.A., Amador, L.A., Rodriguez, A.D., Jankowsky, E., and Pelletier, J. (2020). A comparative study of small molecules targeting eIF4A. RNA *26*, 541–549.

Naineni, S.K., Liang, J., Hull, K., Cencic, R., Zhu, M., Northcote, P., Teesdale-Spittle, P., Romo, D., Nagar, B., and Pelletier, J. (2021). Functional mimicry revealed by the crystal structure of an eIF4A:RNA complex bound to the interfacial inhibitor, desmethyl pateamine A. Cell Chem. Biol. *28*, 825–834.e6.

Novac, O., Guenier, A.S., and Pelletier, J. (2004). Inhibitors of protein synthesis identified by a high throughput multiplexed translation screen. Nucleic Acids Res. *32*, 902–915.

Oblinger, J.L., Burns, S.S., Akhmametyeva, E.M., Huang, J., Pan, L., Ren, Y., Shen, R., Miles-Markley, B., Moberly, A.C., Kinghorn, A.D., et al. (2016). Components of the eIF4F complex are potential therapeutic targets for malignant peripheral nerve sheath tumors and vestibular schwannomas. Neuro-oncol. *18*, 1265–1277.

Oh, Y.S., Kim, D.G., Kim, G., Choi, E.C., Kennedy, B.K., Suh, Y., Park, B.J., and Kim, S. (2010). Downregulation of lamin A by tumor suppressor AIMP3/p18 leads to a progeroid phenotype in mice. Aging Cell *9*, 810–822.

Park, B.J., Kang, J.W., Lee, S.W., Choi, S.J., Shin, Y.K., Ahn, Y.H., Choi, Y.H., Choi, D., Lee, K.S., and Kim, S. (2005). The haploinsufficient tumor suppressor p18 upregulates p53 via interactions with ATM/ATR. Cell *120*, 209–221.

Peters, T.L., Tillotson, J., Yeomans, A.M., Wilmore, S., Lemm, E., Jiménez-Romero, C., Amador, L.A., Li, L., Amin, A.D., Pongtornpipat, P., et al. (2018). Target-based screening against eIF4A1 reveals the marine natural product elatol as a novel inhibitor of translation initiation with *in vivo* antitumor activity. Clin. Cancer Res. *24*, 4256–4270.

Proksch, P., Giaisi, M., Treiber, M.K., Palfi, K., Merling, A., Spring, H., Krammer, P.H., and Li-Weber, M. (2005). Rocaglamide derivatives are immunosuppressive phytochemicals that target NF-AT activity in T cells. J. Immunol. *174*, 7075–7084.

Quevillon, S., and Mirande, M. (1996). The p18 component of the multisynthetase complex shares a protein motif with the β and γ subunits of eukaryotic elongation factor 1. FEBS Lett. *395*, 63–67.

Quevillon, S., Robinson, J.C., Berthonneau, E., Siatecka, M., and Mirande, M. (1999). Macromolecular assemblage of aminoacyl-tRNA synthetases: Identification of protein-protein interactions and characterization of a core protein. J. Mol. Biol. *285*, 183–195.

Robichaud, N., Sonenberg, N., Ruggero, D., and Schneider, R.J. (2019). Translational control in cancer. Cold Spring Harb. Perspect. Biol. *11*, a032896.

Robinson, M.M., Dasari, S., Konopka, A.R., Johnson, M.L., Manjunatha, S., Esponda, R.R., Carter, R.E., Lanza, I.R., and Nair, K.S. (2017). Enhanced protein translation underlies improved metabolic and physical adaptations to different exercise training modes in young and old humans. Cell Metab. *25*, 581–592.

Rubio, C.A., Weisburd, B., Holderfield, M., Arias, C., Fang, E., DeRisi, J.L., and Fanidi, A. (2014). Transcriptome-wide characterization of the eIF4A signature highlights plasticity in translation regulation. Genome Biol. *15*, 476.

Ryu, I., Won, Y.-S., Ha, H., Kim, E., Park, Y., Kim, M.K., Kwon, D.H., Choe, J., Song, H.K., Jung, H., and Kim, Y.K. (2019). eIF4A3 phosphorylation by CDKs affects NMD during the cell cycle. Cell Rep. *26*, 2126–2139.e9.

Sabapathy, K. (2012). Role of the JNK pathway in human diseases. Prog. Mol. Biol. Transl. Sci. *106*, 145–169.

Saradhi, U.V., Gupta, S.V., Chiu, M., Wang, J., Ling, Y., Liu, Z., Newman, D.J., Covey, J.M., Kinghorn, A.D., Marcucci, G., et al. (2011). Characterization of silvestrol pharmacokinetics in mice using liquid chromatography-tandem mass spectrometry. AAPS J. *13*, 347–356.

Schatz, J.H., Oricchio, E., Wolfe, A.L., Jiang, M., Linkov, I., Maragulia, J., Shi, W., Zhang, Z., Rajasekhar, V.K., Pagano, N.C., et al. (2011). Targeting cap-dependent translation blocks converging survival signals by AKT and PIM kinases in lymphoma. J. Exp. Med. *208*, 1799–1807.

Schulz, G., Victoria, C., Kirschning, A., and Steinmann, E. (2021). Rocaglamide and silvestrol: A long story from anti-tumor to anti-coronavirus compounds. Nat. Prod. Rep. *38*, 18–23.

Schwanhäusser, B., Busse, D., Li, N., Dittmar, G., Schuchhardt, J., Wolf, J., Chen, W., and Selbach, M. (2011). Global quantification of mammalian gene expression control. Nature *473*, 337–342.

Shen, L., and Pelletier, J. (2020). Selective targeting of the DEAD-box RNA helicase eukaryotic initiation factor (eIF) 4A by natural products. Nat. Prod. Rep. *37*, 609–616.

Steinberger, J., Shen, L., J Kiniry, S., Naineni, S.K., Cencic, R., Amiri, M., Aboushawareb, S.A.E., Chu, J., Maïga, R.I., Yachnin, B.J., et al. (2020). Identification and characterization of hippuristanol-resistant mutants reveals eIF4A1 dependencies within mRNA 5′ leader regions. Nucleic Acids Res. *48*, 9521–9537.

Thompson, P.A., Eam, B., Young, N.P., Fish, S., Chen, J., Barrera, M., Howard, H., Sung, E., Parra, A., Staunton, J., et al. (2021). Targeting oncogene mRNA translation in B-cell malignancies with eFT226, a potent and selective inhibitor of eIF4A1. Mol. Cancer Ther. *20*, 26–36.

Todt, D., Moeller, N., Praditya, D., Kinast, V., Friesland, M., Engelmann, M., Verhoye, L., Sayed, I.M., Behrendt, P., Dao Thi, V.L., et al. (2018). The natural compound silvestrol inhibits hepatitis E virus (HEV) replication in vitro and in vivo. Antiviral Res. *157*, 151–158.

Townsend, E.C., Murakami, M.A., Christodoulou, A., Christie, A.L., Köster, J., DeSouza, T.A., Morgan, E.A., Kallgren, S.P., Liu, H., Wu, S.C., et al. (2016). The public repository of xenografts enables discovery and randomized phase II-like trials in mice. Cancer Cell *30*, 183.

Truitt, M.L., and Ruggero, D. (2016). New frontiers in translational control of the cancer genome. Nat. Rev. Cancer *16*, 288–304.

Vogel, C., and Marcotte, E.M. (2012). Insights into the regulation of protein abundance from proteomic and transcriptomic analyses. Nat. Rev. Genet. *13*, 227–232.

Wagner, E.F., and Nebreda, A.R. (2009). Signal integration by JNK and p38 MAPK pathways in cancer development. Nat. Rev. Cancer *9*, 537–549.

Wang, Z.Y., Leushkin, E., Liechti, A., Ovchinnikova, S., Mößinger, K., Brüning, T., Rummel, C., Grützner, F., Cardoso-Moreira, M., Janich, P., et al. (2020). Transcriptome and translatome co-evolution in mammals. Nature *588*, 642–647.

Weston, C.R., and Davis, R.J. (2007). The JNK signal transduction pathway. Curr. Opin. Cell Biol. *19*, 142–149.

Wiegering, A., Uthe, F.W., Jamieson, T., Ruoss, Y., Hüttenrauch, M., Küspert, M., Pfann, C., Nixon, C., Herold, S., Walz, S., et al. (2015). Targeting translation initiation bypasses signaling crosstalk mechanisms that maintain high MYC levels in colorectal cancer. Cancer Discov. *5*, 768–781.

Wolfe, A.L., Singh, K., Zhong, Y., Drewe, P., Rajasekhar, V.K., Sanghvi, V.R., Mavrakis, K.J., Jiang, M., Roderick, J.E., Van der Meulen, J., et al. (2014). RNA G-quadruplexes cause eIF4A-dependent oncogene translation in cancer. Nature *513*, 65–70.

Zhao, W., Li, J., Chen, M.M., Luo, Y., Ju, Z., Nesser, N.K., Johnson-Camacho, K., Boniface, C.T., Lawrence, Y., Pande, N.T., et al. (2020). Large-scale characterization of drug responses of clinically relevant proteins in cancer cell lines. Cancer Cell *38*, 829–843.e4.

Zhu, J.Y., Lavrik, I.N., Mahlknecht, U., Giaisi, M., Proksch, P., Krammer, P.H., and Li-Weber, M. (2007). The traditional Chinese herbal compound rocaglamide preferentially induces apoptosis in leukemia cells by modulation of mitogen-activated protein kinase activities. Int. J. Cancer *121*, 1839–1846.

STAR★METHODS

KEY RESOURCES TABLE

REAGENT or RESOURCE	SOURCE	IDENTIFIER
Antibodies		
Puromycin	Kerafast	Cat#Equation 0001; RRID: AB_2620162
eIF4A1	Abcam	Cat#31217; RRID: AB_732122
eIF4A2	SCBT	Cat#sc-137148; RRID:AB_2097384
CD98hc	CST	Cat#13180S; RRID:AB_2687475
GEF-H1	Proteintech	Cat#24472-1-AP; RRID:AB_2879560
CEP170	ThermoFisher Scientific	Cat#41-3200; RRID:AB_2533502
DHX36	Proteintech	Cat#13159-1-AP; RRID:AB_2092157
DDX39	Proteintech	Cat#11723-1-AP; RRID:AB_10858318
JNK	CST	Cat#4672S; RRID:AB_330915
Phospho-JNK	CST	Cat#4668S; RRID:AB_823588
c-JUN	CST	Cat#9165S; RRID:AB_2130165
Phospho-c-JUN	CST	Cat#9261S; RRID:AB_2130162
RHOA	CST	Cat#2117S; RRID:AB_10693922
RHO	ThermoFisher Scientific	Cat#16116
p130Ca	CST	Cat#13846S; RRID:AB_2798328
Phospho-p130Cas	CST	Cat#4011S; RRID:AB_2274823
AKT	CST	Cat#4685S; RRID:AB_2225340
Phospho-AKT	CST	Cat#4060S; RRID:AB_2315049
MCL-1	CST	Cat#94296S; RRID:AB_2722740
CPSF73	Proteintech	Cat#11609-1-AP; RRID:AB_2292188
eEF1ε1	Proteintech	Cat#10805-1-AP; RRID:AB_2097140
DDX17	Proteintech	Cat#19910-1-AP; RRID:AB_10667004
PABPN1	Proteintech	Cat#66807-1-Ig; RRID:AB_2882150
Histone H3	CST	Cat#4499S; RRID:AB_10544537
PABPN1	Proteintech	Cat#66807-1-Ig; RRID:AB_2882150
GAPDH	CST	Cat#5174T; RRID:AB_10622025
CYPB	ThermoFisher Scientific	Cat#PA1-027A; RRID:AB_2169138
Cleaved caspase-3 antibody	CST	Cat#9664S; RRID:AB_2070042
Goat anti-rabbit IgG, HRP-linked	CST	Cat#7074S; RRID:AB_2099233
Horse anti-mouse IgG, HRP-linked	CST	Cat#7076S; RRID:AB_330924
Goat anti-rabbit IgG Antibody (H+L), biotinylated	Vector Laboratories	Cat#BP-9100-50; RRID:AB_2827937
Biological samples		
Patient derived Glioblastoma PDX	Sylvester Comprehensive Cancer Center, Miller School of Medicine, University of Miami, from a Grade IV relapse tumor excised from the brain of a female patient.	N/A
Patient Derived DLBCL PDX	tumor (germinal-center B cell (GCB) subtype) excised from the spleen of a 57-year-old male with no prior history of treatment (Townsend et al., 2016)	N/A
Chemicals, peptides, and recombinant proteins		
Silvestrol	MedChemExpress	Cat#HY-13251
Rocaglamide A	MedChemExpress	Cat#HY-19356
Zotatifin	MedChemExpress	Cat#HY-112163

(Continued on next page)

Continued

REAGENT or RESOURCE	SOURCE	IDENTIFIER
JNK-IN-8	MedChemExpress	Cat#HY-13319
JPH203	MedChemExpress	Cat#HY-100868
Actinomycin D	Millipore-Sigma.	Cat#
RIPA buffer	ThermoFisher Scientific	Cat#89900
Protease inhibitor Cocktail	Millipore-Sigma	Cat#5892791001
Critical commercial assays		
Active Rho Pull-down and Detection Kit	ThermoFisher Scientific	Cat#16116
PE Annexin V Apoptosis Detection Kit I	BD Biosciences	Cat#559763
NovaRED substrate kit Peroxidase (HRP)	Vector Laboratories	Cat#SK4800
Maxima H Minus cDNA Synthesis Master Mix	ThermoFisher Scientific	Cat#M1661
PowerUp™ SYBR® Green Master Mix	ThermoFisher Scientific	Cat#A25742
TMT10plex™ Isobaric Label Reagent Set	ThermoFisher Scientific	Cat#90110
Deposited data		
Mass spectrometry data	PRIDE via ProteomeXchange	PXD022556
Experimental models: Cell lines		
Human U87MG cell line	American Type Culture Collection	Cat#HTB-14
Human HeLa cell line	American Type Culture Collection	Cat#CCL-2
Human MDA-MB-468 cell line	American Type Culture Collection	Cat#HTB-132
Human BJAB cell line	DSMZ	Cat#ACC757
Experimental models: Organisms/strains		
NOD scid gamma mice	The Jackson Laboratory	N/A
Oligonucleotides		
CD98hc (Forward 5′- TGCAGCTGGAG TTTGTCTC −3′; Reverse 5′- CCTGGC AGGGTGAAGAG −3′)	This paper	N/A
GEF-H1 (Forward 5′- TGGCTGCCTGC TCTGGAAGAC −3′; Reverse 5′- AGGC TTGTCCAGGGTAGGAAAG −3′)	This paper	N/A
SPEN (Forward 5′- TGGCCCTGGTTCT CTACAATGAAA −3′; Reverse 5′- TGC CCTTCGTTCCTCTCTTCTT −3′)	This paper	N/A
CEP170 (Forward 5′- GTGCAGCACAA AACTACTG −3′; Reverse 5′- TGACG GCTGCCCATATAA −3′)	This paper	N/A
eIF4A2 (Forward 5′- TGACCCTTGAA GGAATCAAAC −3′; Reverse 5′- TGT CTCGTACAAGTCACAAAG −3′)	This paper	N/A
DHX36 (Forward 5′- AACGACGAGAA GAACAAAT −3′; Reverse 5′- GAGC ATGGTGTGTTCTTAGTA −3′)	This paper	N/A
DDX39 (Forward 5′- GCGCCACCCTG AGCAAGGACA −3′; Reverse 5′- GGC CGTGCAGCGTGAGCTT −3′)	This paper	N/A
Human tRNA primer sequences: initiator methionine tRNA (Forward 5′- GCAGAG TGGCGCAGCGGAAGCGTG - 3′; Reverse 5′- TAGCAGAGGATGGTTTCG - 3′)	This paper	N/A
Additional oligonucleotides can be found in Table S3		

(Continued on next page)

Continued

REAGENT or RESOURCE	SOURCE	IDENTIFIER
Recombinant DNA		
ARHGEF2 ORF cDNA construct and empty vector	GenScript	Cat#OHu26696
Software and algorithms		
PEAKS X+ (v10.5)	Bioinformatics Solutions Inc. in Waterloo, Ontario, Canada.	https://www.bioinfor.com/download-peaks-studio/
Visualization and Integrated Discovery (DAVID) bioinformatics resource (v6.8).	online	https://david.ncifcrf.gov
Other		
Thermo Scientific Orbitrap Fusion-Lumos Tribid Mass Spectrometer (CA)	ThermoFisher, San Jose,	N/A
Nanospray source and Dionix Ultimate 1000 nano-LC system	ThermoFisher, San Jose, CA	N/A

RESOURCE AVAILABILITY

Lead contact
Further information and requests for resources and reagents should be directed to and will be fulfilled by the lead contact, Jonathan H. Schatz (jschatz@med.miami.edu)

Materials availability
Materials generated from this study, such as plasmids and cell lines, will be made available upon requests made to the lead contact.

Data availability
Mass spectrometry proteomics data are deposited in the PRIDE repository and available via ProteomeXchange with identifier PXD022556.

This paper does not report original code.

Any additional information required to reanalyze the data reported in this paper is available from the lead contact upon request.

EXPERIMENTAL MODEL AND SUBJECT DETAILS

Cell culture and reagents
Human cell lines U87MG (#HTB-14), HeLa (#CCL-2), and MDA-MB-468 (HTB-132) were purchased from the American Type Culture Collection and propagated in DMEM with 10% FBS and 1% penicillin-streptomycin. Human cell line BJAB (#ACC757) was purchased from DSMZ and propagated in RPMI-1640 with 10% FBS and 1% penicillin-streptomycin. Cells were maintained at 37 °C in a 5% CO_2 humidified incubator. Silvestrol (#HY-13251), rocaglamide A (#HY-19356), zotatifin (#HY-112163), JNK-IN-8 (#HY-13319), and JPH203 (#HY-100868) were purchased from MedChemExpress, actinomycin D (#A1410) was purchased from Millipore-Sigma.

Mice
All animal studies were performed under the approval of the University of Miami Institutional Animal Care and Use committee. PDX tumor models were engrafted in male NOD scid gamma mice > 8 weeks of age (The Jackson Laboratory) through surgical dorsal tumor implantation. Criterion for enrollment was tumor volume > 300 mm³ measured by ultrasound (Vevo 3100, Visualsonics). Mice were dosed with silvestrol (1 mg/kg in 20% 2-hydroxypropyl-β-cyclodextrin) or vehicle via intraperitoneal injection daily for three days and euthanized at the predetermined endpoint of eight hr after the final injection. The mice were housed within a barrier facility. All equipment, food, or bedding which comes in contact with the animals is autoclaved, irradiated (food), or chemically disinfected. All cages are handled under animal transfer stations (Biological Safety Cabinets). Rodents are housed in individually ventilated, double sided, racks (Allentown) and are changed weekly. The mice were housed socially (2 or more per cage) with enrichment.

Patient-derived xenograft (PDX) tumors
Glioblastoma PDX was established at the Sylvester Comprehensive Cancer Center, Miller School of Medicine, University of Miami, from a Grade IV relapse tumor excised from the brain of a 38-year-old female patient. DLBCL PDX was established from a tumor (germinal-center B cell (GCB) subtype) excised from the spleen of a 57-year-old male with no prior history of treatment (Townsend et al., 2016).

METHOD DETAILS

Pulse SILAC (pSILAC)

Cells were grown in light (R_0K_0) SILAC media (AthenaES) for 7 days and pulsed with heavy ($R_{10}K_8$) SILAC media (AthenaES) for the last 8 hr (TMT-pSILAC) or 4 hr (MATRIX) of silvestrol treatment.

Ribosome density profiling

Briefly, cells were treated with 0.1 mg/ml of cycloheximide for the last 10 min of treatment, followed by ice-cold washes with PBS$^{-/-}$ containing cycloheximide (0.1 mg/ml). Cells were then lysed in polysome lysis buffer (0.3 M NaCl, 15 mM MgCl$_2$.6H$_2$O, 15 mM Tris-HCl pH 7.4, 1% Triton X-100, 0.1 mg/ml cycloheximide, 100 units/ml RNase inhibitor). Following centrifugation (twice at 10,000 g for 5 min at 4 °C) to remove cellular debris, samples were loaded based on equal total RNA onto a 10%–50% sucrose gradient, and subjected to ultracentrifugation (187,813 g for 1.5 hr at 4 °C) using a SW 41 Ti rotor (Beckman Coulter). Samples were then fractionated into 1 ml fractions and collected using the BR-188 density gradient fractionation system (Brandel). Total RNA was isolated from each fraction by phenol-chloroform extraction and ethanol precipitation following proteinase K treatment. Total protein was isolated by TCA precipitation (20% final TCA concentration) followed by three ice-cold acetone washes. Three independent experiments were pooled into a single sample for MATRIX MS analysis.

TMT-pSILAC mass spectrometry
TMT labeling and fractionation

MS sample preparation and runs were performed at Bioinformatics Solutions Inc. (Waterloo, Ontario, Canada). Samples were reduced, alkylated, digested, and TMT labeled using the TMT10plex^{TM} Isobaric Label Reagent Set (ThermoFisher Scientific, #90110) according to manufacturer's directions. Labeled peptides from all samples were combined and lyophilized. Peptides were then resuspended in 20 μL of ddH$_2$O and subjected to high pH reversed-phase HPLC fractionation using a Waters XBridge C18 column. A linear gradient of Buffer A (ddH$_2$O, pH = 10) to 40% Buffer B (80% acetonitrile, pH = 10) was used to fractionate peptides. Fractions were collected starting 2 min into the 90 min gradient, in 2 min time intervals for a total of 44 fractions.

LC-MS/MS analysis

Each of the 44 high pH fractions were lyophilized, resuspended in 0.1% formic acid, and loaded onto a 96-well plate for injection into the mass spectrometer. Samples were analyzed on a Thermo Scientific Orbitrap Fusion-Lumos Tribid Mass Spectrometer (Thermo-Fisher, San Jose, CA) outfitted with a nanospray source and Dionix Ultimate 1000 nano-LC system (ThermoFisher, San Jose, CA) Peptide mixtures were loaded into a PEPMAP100 C18 5 μM trap column (ThermoFisher, San Jose, CA) at a constant flow of 30 μL/min. Peptides were eluted and focused using a PEPMAP C18 2 μM 15 cm column (ThermoFisher, San Jose, CA) over the course of a 60 min gradient. 0 - 48 min:4% - 35% acetonitrile + 0.1% formic acid; 48 - 55 min of 90% acetonitrile + 0.1% formic acid for column cleaning, 55 - 60 min of 4% acetonitrile + 0.1% formic acid for column equilibration. Peptides were introduced by nano-electrospray into the mass spectrometer. Data was acquired using the MultiNotch MS3 acquisition with synchronous precursor selection (SPS) with a cycle time of 2 s. MS1 acquisition was performed with a scan range of 550 m/z - 1800 m/z with resolution set to 120 000, maximum injection time of 50 ms and AGC target set to 4e5. Isolation for MS2 scans was performed in the quadrupole, with an isolation window of 0.7. MS2 scans were done in the linear ion trap with a maximum injection time of 50 ms and a normalized collision energy of 35%. For MS3 scans, HCD was used, with a collision energy of 65% and scans were measured in the orbitrap with a resolution of 50000, a scan range of 100 m/z - 300 m/z, an AGC Target of 1e5, and a maximum injection time of 50 ms. Dynamic exclusion was applied using a exclusion list of one repeat count with an exclusion duration of 30 s. All LC-MS/MS was performed at Bioinformatics Solutions Inc. in Waterloo, Ontario, Canada.

MS data analysis

MS raw files were processed using PEAKS X+ (v10.5, Bioinformatics Solutions Inc.). The data was searched against the Human Uniprot database consisting of reviewed canonical sequences (total entry 20332). Parent mass tolerance was set to 10ppm, with fragment mass tolerance of 0.6 Da. Semi-specific tryptic cleavage was selected with allows for a maximum of 2 missed cleavages. For identification of all proteins, fixed modifications of TMT (229.16 Da) on peptide N-terminal and carbamidomethylation (57.02 Da) on cysteine residues were specified. Variable modifications of TMT on a "light" lysine (229.16 Da), TMT on a "heavy" lysine (237.18 Da), 13C(6)15N(2) SILAC Label on lysine, 13C(6)15N(4) SILAC label on arginine, as well as oxidation (15.99 Da) on methionine were specified. For identification of only heavy labeled proteins, fixed modifications included carbamidomethylation (57.02 Da) on cysteine, TMT on a "heavy" lysine (237.18 Da), TMT (229.16 Da) on peptide N-terminal, and 13C(6)15N(4) SILAC label on arginine were selected, while a variable modification of Oxidation (15.99 Da) on Methionine was also included. TMT quantification was also performed using the PEAKS X+ quantification module, allowing a mass tolerance of 20 ppm and quantifying all peptides that pass a 1% FDR threshold.

MATRIX mass spectrometry
TMT labeling and fractionation

MS sample preparation and runs were performed at Bioinformatics Solutions Inc. (Waterloo, Ontario, Canada). Samples were reduced, alkylated, digested, and TMT labeled using the TMT10plex^{TM} Isobaric Label Reagent Set (ThermoFisher Scientific,

#90110) according to manufacturer's directions. Labeled peptides from all samples were combined and lyophilized. Peptides were then resuspended in 20 μL of ddH$_2$O and subjected to high pH reversed-phase HPLC fractionation using a Waters XBridge C18 column. A linear gradient of Buffer A (ddH$_2$O pH = 10) to 40% Buffer B (80% acetonitrile, pH = 10) was used to fractionate peptides. Fractions were collected starting 2 min into the 90 min gradient, in 2 min time intervals for a total of 44 fractions.

LC-MS/MS analysis

Each of the 44 high pH fractions were lyophilized, resuspended in 0.1% formic acid, and loaded onto a 96-well plate for injection into the mass spectrometer. Samples were analyzed on a Thermo Scientific Orbitrap Fusion-Lumos Tribid Mass Spectrometer (ThermoFisher, San Jose, CA) outfitted with a nanospray source and Dionix Ultimate 1000 nano-LC system (ThermoFisher, San Jose, CA) Peptide mixtures were loaded into a PEPMAP100 C18 5 μM trap column (ThermoFisher, San Jose, CA) at a constant flow of 30 μL/min. Peptides were eluted and focused using a PEPMAP C18 2 μM 15 cm column (ThermoFisher, San Jose, CA) over the course of a 60 min gradient. 0 - 48 min:4% - 35% acetonitrile + 0.1% formic acid; 48 - 55 min of 90% acetonitrile + 0.1% formic acid for column cleaning, 55 - 60 min of 4% acetonitrile + 0.1% formic acid for column equilibration. Peptides were introduced by nano-electrospray into the mass spectrometer. Data was acquired using the MultiNotch MS3 acquisition with synchronous precursor selection (SPS) with a cycle time of 2 s. MS1 acquisition was performed with a scan range of 550 m/z - 1800 m/z with resolution set to 120 000, maximum injection time of 50 ms and AGC target set to 4e5. Isolation for MS2 scans was performed in the quadrupole, with an isolation window of 0.7. MS2 scans were done in the linear ion trap with a maximum injection time of 50 ms and a normalized collision energy of 35%. For MS3 scans, HCD was used, with a collision energy of 65% and scans were measured in the orbitrap with a resolution of 50000, a scan range of 100 m/z - 300 m/z, an AGC Target of 1e5, and a maximum injection time of 50 ms. Dynamic exclusion was applied using a exclusion list of one repeat count with an exclusion duration of 30 s. All LC-MS/MS was performed at Bioinformatics Solutions Inc. in Waterloo, Ontario, Canada.

MS data analysis

MS raw files were processed using PEAKS X+ (v10.5, Bioinformatics Solutions Inc.). The data was searched against the Human Uniprot database consisting of reviewed canonical and isoform sequences (total entry 42339). Parent mass tolerance was set to 20 ppm, with fragment mass tolerance of 0.6Da. Semi-specific tryptic cleavage was selected with allows for a maximum of 2 missed cleavages. Fixed modifications of TMT (229.16 Da) on lysine and peptide N-terminal and carbamidomethylation (57.02 Da) on cysteine residues were specified. Variable modifications of deamidation (0.98 Da) on asparagine and glutamine, as well as oxiation (15.99 Da) on methionine were specified. TMT quantification was also performed using the PEAKS X+ quantification module, allowing a mass tolerance of 20 ppm and quantifying all peptides that pass a 1% FDR threshold.

RNA interference

Target-specific pools of four independent small interfering RNA (siRNA) species against human CD98hc (M-003542-02), GEF-H1 (M-009883-01), GEF-H1 3′-UTR (CTM-651415, CTM-651416), eIF4A1 (M-020178-01), eIF4A2 (M-013758-01), CPSF73 (M-006365-00), eEF1ε1 (M-015983-01), and non-targeting siRNA control pool #1 (D-001206-13) (siGENOME SMARTpool) were purchased from Dharmacon (Horizon Discovery). siRNA pools were transfected using Effectene (QIAGEN) at a final concentration of 50 nM for 48 hr unless otherwise stated before subsequent treatments. ARHGEF2/GEF-H1 ORF cDNA construct (OHu26696) and empty vector were purchased from GenScript, and transfected using Effectene (QIAGEN) following manufacturer protocols.

Active RHO pull-down

RHO-GTP pull-down was performed using the Active RHO Pull-down and Detection Kit (ThermoFisher Scientific #16116) according to the manufacturer's protocols, using 1 mg of input cell lysate per condition.

Subcellular fractionation

Briefly, cells were washed twice with ice-cold PBS in the presence of protease inhibitors (ThermoFisher Scientific, #78430), and then lysed with 0.1% NP-40 (Calbiochem). After trituration, an aliquot of the lysate was removed (whole-cell lysate) immediately, mixed with 4X Laemmli buffer, and stored on ice. Following centrifugation (pulse-spin for 10 sec) of the remaining cell lysate, an aliquot of the supernatant was removed (cytoplasmic fraction), mixed with 4X Laemmli buffer, boiled, and stored at $-80\,^\circ$C. Nuclei pellet was resuspended with 0.1% NP-40, centrifuged to remove supernatant, and resuspended in 4X Laemmli buffer. Nuclei pellet and whole-cell lysate were then sonicated (20 kHz, 2 pulses, 8 sec each), and stored at $-80\,^\circ$C.

Gene Ontology (GO) pathway enrichment

GO enrichment analysis was performed using the online Database for Annotation, Visualization and Integrated Discovery (DAVID) bioinformatics resource (v6.8).

Cell viability and apoptosis

Cell viability was assessed by luminescence measurements using CellTiter-Glo® and RealTime-Glo MT viability assays (Promega). Apoptosis was assessed by standard flow cytometry using the PE Annexin V Apoptosis Detection Kit I (BD Biosciences, #559763).

CellPress
OPEN ACCESS

Immunohistochemistry

Formalin-fixed, paraffin-embedded tumor and organ sections were cut at 4 μm using the HistoCore Autocut microtome (Leica). Slides were deparaffinized and incubated in 3% H_2O_2 for 10 min. Heat induced epitope retrieval was performed by immersing the slides into 10 mM citrate buffer for 15 min in a pressure cooker at 15 psi. Slides were blocked with 10% goat serum in sterile 1X PBS for 1 hr at room temperature in a humidified chamber followed by three PBS washes (5 min each). Primary and secondary antibody incubations were performed in 1% BSA in sterile 1X PBS overnight at 4°C, and 1 hr at room temperature, respectively. Three PBS washes (5 min each) were performed after each incubation. Primary antibodies: phospho-JNK (CST #4668S, 1:50); GEF-H1 (Proteintech #24472-1-AP, 1:200); eIF4A2 (SCBT #sc-137148, 1:100); cleaved caspase-3 antibody (CST #9664S, 1:200 dilution). Secondary antibody: goat anti-rabbit IgG Antibody (H+L), biotinylated and ready-to-use (Vector Laboratories #BP-9100-50). Chromogen visualization was realized using the NovaRED substrate kit Peroxidase (HRP) (Vector Laboratories #SK4800). Nuclei were counterstained with hematoxylin. Images were captured with a maximum range of 40X using a Slideview VS200 digital slide scanner (Olympus).

For total protein extraction, flash frozen tumors samples were thawed on dry ice, homogenized with a rubber stopper in 100 μL of RIPA buffer (ThermoFisher #89900) containing protease inhibitors (Millipore-Sigma #5892791001), and sonicated at high setting for 10 cycles of 30 s pulses at 4°C (Bioruptor® 300, Diagenode). Samples were then centrifuged for 10 min at 15,000 g, and supernatants were collected for immunoblot analysis.

Protein extraction from mouse tumors

For total protein extraction, flash frozen tumors samples were thawed on dry ice, homogenized with a rubber stopper in 100 μL of RIPA buffer (ThermoFisher #89900) containing protease inhibitors (Millipore-Sigma #5892791001), and sonicated at high setting for 10 cycles of 30 s pulses at 4°C (Bioruptor® 300, Diagenode). Samples were then centrifuged for 10 min at 15,000 g, and supernatants were collected for immunoblot analysis.

Immunoblot

SDS-PAGE was performed on Bolt™ 4%–12% Bis-Tris Plus pre-made gels (ThermoFisher Scientific) using the Mini Gel Tank system (ThermoFisher Scientific), and transferred to 0.2 μm Immuno-Blot® PVDF membranes (Bio-Rad) using the Bolt™ Mini Blot Module (ThermoFisher Scientific), all according to the manufacturer's protocols. Chemiluminescent signals were captured using a digital chemiluminescent imaging system. Densitometry was performed on non-saturated signals using ImageJ (NIH), and normalized to loading control. Primary antibodies: puromycin (Kerafast #Equation 0001, 1:1000); eIF4A1 (Abcam #31217, 1:1000); eIF4A2 (SCBT #sc-137148, 1:1000); CD98hc (CST #13180S, 1:500); GEF-H1 (Proteintech #24472-1-AP, 1:1000); SPEN (Novus Biologicals #NB100-58799); CEP170 (ThermoFisher Scientific #41-3200, 1:1000); DHX36 (Proteintech #13159-1-AP, 1:1000); DDX39 (Proteintech #11723-1-AP, 1:1000); JNK (CST #4672S, 1:1000); phospho-JNK (CST #4668S, 1:1000); c-JUN (CST #9165S, 1:1000); phospho-c-JUN (CST #9261S, 1:1000); RHOA (CST #2117S, 1:1000); RHO (ThermoFisher Scientific #16116, 1:1000); p130Cas (CST #13846S, 1:1000); phospho-p130Cas (CST #4011S, 1:1000); AKT (CST #4685S, 1:1000); phospho-AKT (CST #4060S, 1:1000); MCL-1 (CST #94296S, 1:1000); CPSF73 (Proteintech #11609-1-AP, 1:1000); eEF1ε1 (Proteintech #10805-1-AP, 1:1000); DDX17 (Proteintech #19910-1-AP); PABPN1 (Proteintech #66807-1-Ig); Histone H3 (CST #4499S, 1:2000); GAPDH (CST #5174T, 1:2000); CYPB (ThermoFisher Scientific #PA1-027A, 1:10000). Secondary antibodies: Goat anti-rabbit IgG, HRP-linked (CST #7074S, 1:10000); Horse anti-mouse IgG, HRP-linked (CST #7076S, 1:10000).

qRT-PCR

First-strand cDNA synthesis was performed using the Maxima H Minus cDNA Synthesis Master Mix (ThermoFisher Scientific, #M1661), according to the manufacturer's protocols. qRT-PCR was performed using a StepOnePlus™ Real-Time PCR System (ThermoFisher Scientific). Relative changes in expression were calculated using the comparative Ct (ΔΔCt) method. 18S rRNA was measured as an internal control for changes in RNA levels. All qPCR reactions were performed using PowerUp™ SYBR® Green Master Mix (ThermoFisher Scientific, #A25742) unless otherwise stated.

Primer sequences

Human mRNA primer sequences: CD98hc (Forward 5′- TGCAGCTGGAGTTTGTCTC −3′; Reverse 5′- CCTGGCAGGGTGAAGAG −3′); GEF-H1 (Forward 5′- TGGCTGCCTGCTCTGGAAGAC −3′; Reverse 5′- AGGCTTGTCCAGGGTAGGAAAG −3′); SPEN (Forward 5′- TGGCCCTGGTTCTCTACAATGAAA −3′; Reverse 5′- TGCCCTTCGTTCCTCTCTTCTT −3′); CEP170 (Forward 5′- GTGCAGCACAA AACTACTG −3′; Reverse 5′- TGACGGCTGCCCATATAA −3′); eIF4A2 (Forward 5′- TGACCCTTGAAGGAATCAAAC −3′; Reverse 5′- TGTCTCGTACAAGTCACAAAG −3′); DHX36 (Forward 5′- AACGACGAGAAGAACAAAT −3′; Reverse 5′- GAGCATGGTGTGTTCTTAG TA −3′); DDX39 (Forward 5′- GCGCCACCCTGAGCAAGGACA −3′; Reverse 5′- GGCCGTGCAGCGTGAGCTT −3′). Human pre-mRNA primer sequences: CD98hc (Forward 5′- TGTGGCCACCAAGGTGAAGG −3′; Reverse 5′- ACAGGGCTTGCTGTGAAAGG −3′); GEF-H1 (Forward 5′- AGGGCCCCACGAGTTTTAG −3′; Reverse 5′- AGGCGGGTCATGATCTTCAG −3′); SPEN (Forward 5′- TGCTTGC TCCTTTCTGATTAAATATT −3′; Reverse 5′- CCGCTCTCGAGGATCTCTATA −3′); CEP170 (Forward 5′- TGCATGGCACATCTTATGA TAC −3′; Reverse 5′- TTCCGGAATCCTTACATCATTC −3′); eIF4A2 (Forward 5′- CCTGCAACAGTTGGAGATT −3′; Reverse 5′- CAACA CGCAAGCAGTTTTTTT −3′); DHX36 (Forward 5′- TACCCTGTGATGTATCCTAAAT −3′; Reverse 5′- GGCAGCTTTTCTCTGAAAT −3′);

DDX39 (Forward 5′- TGCCCTCCCCACCTAGAC −3′; Reverse 5′- CTCGCCCTACTCACATCCTG −3′). MCL-1: TaqMan® gene expression assay ID Hs01050896 (ThermoFisher Scientific). Human tRNA primer sequences: initiator methionine tRNA (Forward 5′- GCAGA GTGGCGCAGCGGAAGCGTG - 3′; Reverse 5′- TAGCAGAGGATGGTTTCG - 3′). eIF4A1: gDNA exon 1 primers: (Forward 5′ – GC CGGAGCGACTAGGAACTA – 3′; Reverse 5′ – CATGAACAATCCACATCCCGC – 3′). eIF4A2: gDNA exon 1 primers: (Forward 5′-GG GGAAAGCGAGGTTTAACTAAC – 3′; Reverse 5′ – GAATATCCACACTGTGCGCC – 3′).

CRISPR-Cas9

U87MG cells were transfected with two plasmids – eSpCas9(1.1)-T2A-GFP-GlntRNA and eSPCas9(1.1)-T2A-mCherry – containing sgRNAs targeting eIF4A2 exons 1 and 2, respectively. 48-hours post-transfection, cells were single-cell sorted into 96-well plates using a FACS Aria Fusion. eIF4A2: exon 1 CRISPR gRNA (5′ – GTTTTTCGGATCATGTCTGG – 3′). eIF4A2: exon 2 CRISPR gRNA (5′ – CTTGTCAGCAGAGAACATGG – 3′).

QUANTIFICATION AND STATISTICAL ANALYSES

All experiments were performed at least three independent times, unless otherwise stated. Statistical analyses were performed in Prism 9 and are indicated in relevant figure legends. Bar plots are displayed as the mean ± standard error of the mean (SEM) unless otherwise noted. Unpaired t tests were performed to determine statistical significance (ns, $p > 0.05$; *$p \leq 0.05$; **$p \leq 0.01$; ***$p \leq 0.001$ and ****$p \leq 0.0001$). For Gene Ontology analyses, false discovery rate was controlled by the Benjamini–Hochberg procedure to produce p values adjusted for multiple comparisons.

Supplemental information

Proteomics reveal cap-dependent

translation inhibitors remodel the

translation machinery and translatome

J.J. David Ho, Tyler A. Cunningham, Paola Manara, Caroline A. Coughlin, Artavazd Arumov, Evan R. Roberts, Ashanti Osteen, Preet Kumar, Daniel Bilbao, Jonathan R. Krieger, Stephen Lee, and Jonathan H. Schatz

Supplemental information

Proteomics Reveal Cap-dependent Translation Inhibitors Remodel the Translation Machinery and Translatome

J.J. David Ho[1,2,3,*,#], Tyler A. Cunningham[1,4,5,*], Paola Manara[1,6], Caroline A. Coughlin[1,4,6], Artavazd Arumov[1,6], Evan R. Roberts[1,7], Ashanti Osteen[1,7], Preet Kumar[1,2], Daniel Bilbao[1,7], Jonathan R. Krieger[8], Stephen Lee[1,9], & Jonathan H. Schatz[1,2,#,†]

Inventory of Supplemental Information

1.
Supplemental Figures
Figure S1, related to Figure 1.
Figure S2, related to Figure 1.
Figure S3, related to Figure 2.
Figure S4, related to Figure 3.
Figure S5, related to Figure 4.
Figure S6, related to Figure 4.
Figure S7, related to Figure 5.
Figure S8, related to Figure 6.

A

U87MG

Silvestrol (nM, 24 hr)

B

U87MG

| | 0 hr | 24 hr | 72 hr | 24 hr recovery | 48 hr recovery |
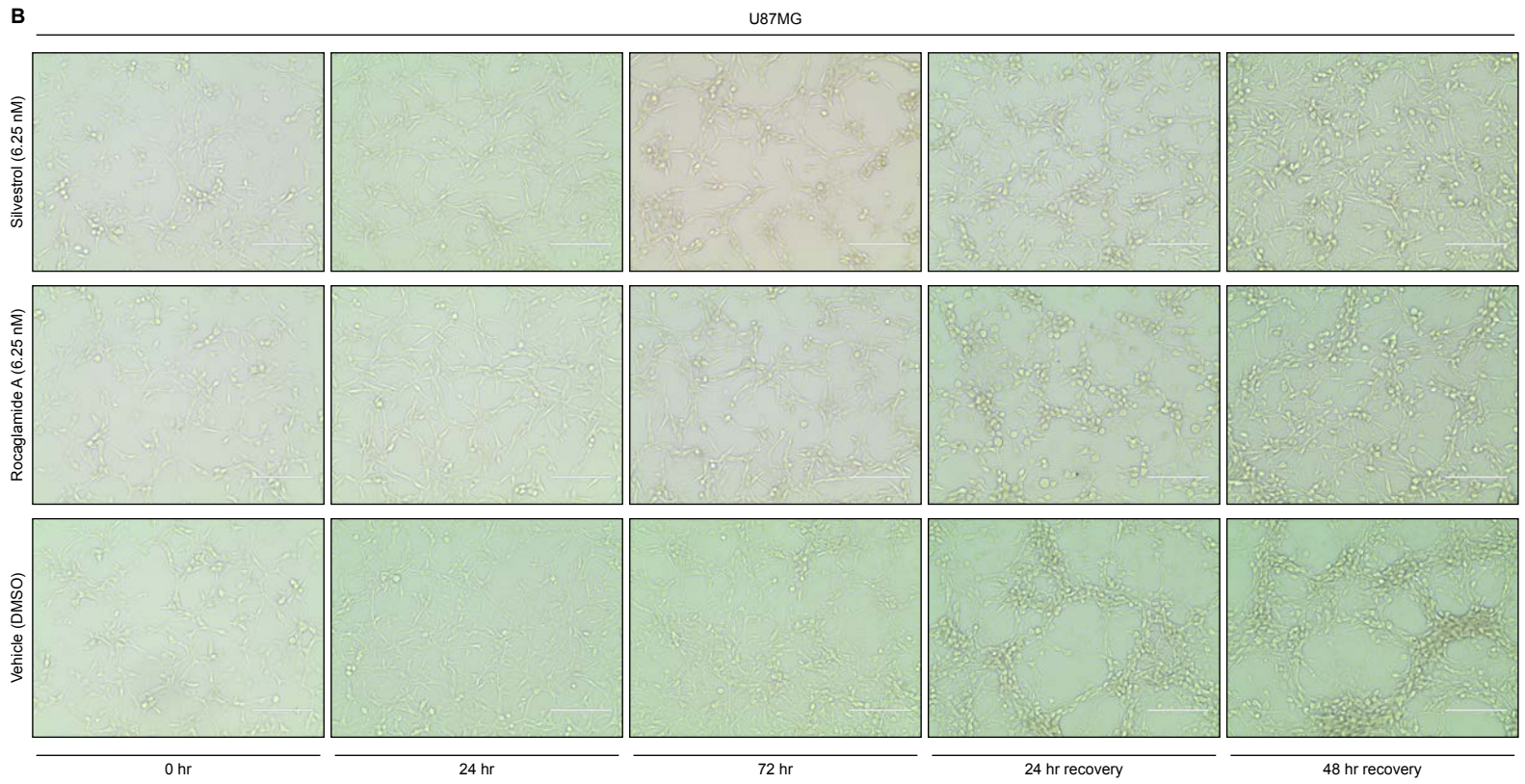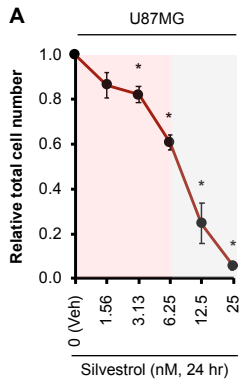
Figure S1.

Figure S1. TMT-pSILAC reveals rocaglate-dependent translatome remodeling, related to Figure 1. (**A**) Relative cell number of U87MG treated with silvestrol (indicated concentrations) or vehicle (DMSO) for 24 hr. Data represent mean ± SEM (error bars) of three independent experiments. Asterisk denotes statistical significance calculated using two-sided Student's t-tests compared to vehicle (DMSO). Pink-shaded area highlights concentrations at which cell viability was largely maintained (> 80%). (**B**) Representative bright field images of U87MG treated with silvestrol (6.25 nM), rocaglamide A (6.25 nM), or DMSO, for 72 hr followed by 48 hr of treatment recovery. Scale bars represent 200 µm.

A

Log$_2$ ratio

4.0   0.0   -4.0

Silvestrol | Vehicle
Rep. #1 | Rep. #2 | Rep. #3 | Rep. #1 | Rep. #2 | Rep. #3

Q8N6M0|OTU6B_HUMAN
P62140|PP1B_HUMAN
Q9NWV8|CSO62_HUMAN
Q16787|LAMA3_HUMAN
Q9H4B7|TBB1_HUMAN
Q5SW79|CE170_HUMAN
O75390|CISY_HUMAN
Q86UQ4|ABCAD_HUMAN
Q9Y5V3|MAGD1_HUMAN
P49327|FAS_HUMAN
P30043|BLVRB_HUMAN
Q14980|NUMA1_HUMAN
Q14240|IF4A2_HUMAN
O15127|SCAM2_HUMAN
P38117|ETFB_HUMAN
Q3ZCM7|TBB8_HUMAN
Q6ZTA4|TRI67_HUMAN
Q8IU68|TMC8_HUMAN
O60784|TOM1_HUMAN
P08195|4F2_HUMAN
P62263|RS14_HUMAN
Q15388|TOM20_HUMAN
Q6NSJ5|ILRC8E_HUMAN
P36542|ATPG_HUMAN
Q9Y6A5|TACC3_HUMAN
A6NJ46|NKX63_HUMAN
P13645|K1C10_HUMAN
Q8WX93|PALLD_HUMAN
Q6VY07|PACS1_HUMAN
P52789|HXK2_HUMAN
Q2M1P5|KIF7_HUMAN
Q9H7Y2|YA001_HUMAN
A6NHN0|OTOL1_HUMAN
Q13596|SNX1_HUMAN
P55786|PSA_HUMAN
Q9BQ39|DDX50_HUMAN
Q14151|SAFB2_HUMAN
P49589|SYCC_HUMAN
P12270|TPR_HUMAN
P41250|SYG_HUMAN
P04264|K2C1_HUMAN
Q9UBT2|SAE2_HUMAN
P05120|PAI2_HUMAN
P06576|ATPB_HUMAN
Q9C0C2|TB182_HUMAN
P50219|MNX1_HUMAN
Q9UEE9|CFDP1_HUMAN
P09525|ANXA4_HUMAN
Q5D1D0|UROL1_HUMAN
Q9H7N4|SFR19_HUMAN
P05455|LA_HUMAN
Q9NR12|PDLI7_HUMAN
O14497|ARI1A_HUMAN
Q96T58|MINT_HUMAN
P49755|TMEDA_HUMAN
O95248|MTMR5_HUMAN
Q5T5Y3|CAMP1_HUMAN
Q92974|ARHG2_HUMAN
Q15046|SYK_HUMAN
Q9Y2Z4|SYYM_HUMAN
Q9Y263|PLAP_HUMAN
Q9P2J5|SYLC_HUMAN
P83881|RL36A_HUMAN
P16070|CD44_HUMAN
P60510|PP4C_HUMAN
P30520|PURA2_HUMAN
Q9UGU0|TCF20_HUMAN
O94830|DDHD2_HUMAN
Q8IUH4|ZDH13_HUMAN
O15069|NACAD_HUMAN
P13535|MYH8_HUMAN
P12883|MYH7_HUMAN

C   PANTHER Overrepresentation Test

Gene Ontology term	Fold enrichment	P value	FDR corrected p
Polymeric cytoskeletal fiber (GO:0099513)	4.07x	4.51e-06	3.02e-03
	e.g. **GEF-H1**		
Extracellular space (GO:0005615)	2.01x	8.86e-05	1.27e-02
	e.g. **CD98hc**		
Aminoacyl-tRNA ligase activity (GO:0004812)	16.2x	6.66e-05	3.90e-02
	CARS, GARS, KARS, LARS, YARS2		

B

Log$_2$ ratio

4.0   0.0   -4.0

Silvestrol | Vehicle
Rep. #1 | Rep. #2 | Rep. #3 | Rep. #1 | Rep. #2 | Rep. #3

Figure S2.

Figure S2. TMT-pSILAC reveals rocaglate-dependent translatome remodeling, related to Figure 1. (**A**) Unsupervised hierarchical clustering of silvestrol-inducible proteins based on TMT-pSILAC analysis. Cell color represents the $\log_2$ ratio to the average abundance across different samples. The following filters were applied: target detected across all 6 samples, fold change ≥ 2, spectrum quality ≥ 10. eIF4A2 (IF4A2) was confirmed as a positive control (highlighted). 72 proteins identified. (**B**) Unsupervised hierarchical clustering of silvestrol-repressed proteins based on TMT-pSILAC. PTGES3 (TEBP) was confirmed as a positive control (highlighted). 165 proteins identified. (**C**) Gene Ontology (GO) pathway enrichment analysis performed on the 101 silvestrol-induced proteins using the PANTHER classification algorithm. P values were calculated using the Fisher's Exact test, and corrected for multiple comparisons using the False Discovery Rate (FDR) method.
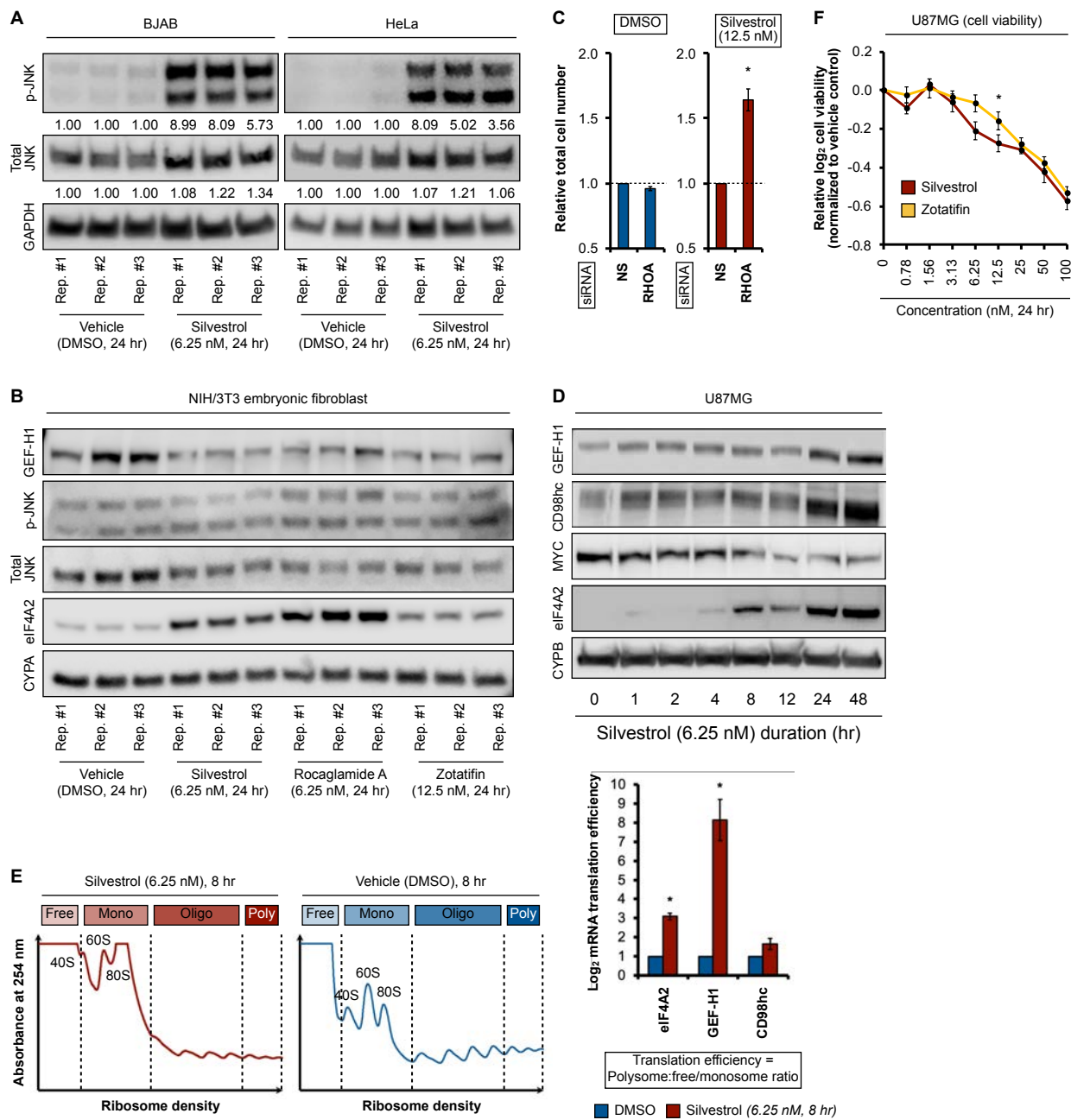
A

BJAB / HeLa

p-JNK
Total JNK
GAPDH

BJAB: 1.00 1.00 1.00 8.99 8.09 5.73 (p-JNK)
1.00 1.00 1.00 1.08 1.22 1.34 (Total JNK)

HeLa: 1.00 1.00 1.00 8.09 5.02 3.56 (p-JNK)
1.00 1.00 1.00 1.07 1.21 1.06 (Total JNK)

Rep. #1 Rep. #2 Rep. #3 Rep. #1 Rep. #2 Rep. #3

Vehicle (DMSO, 24 hr) / Silvestrol (6.25 nM, 24 hr)

B NIH/3T3 embryonic fibroblast

GEF-H1
p-JNK
Total JNK
eIF4A2
CYPA

Rep. #1 Rep. #2 Rep. #3 (×4)

Vehicle (DMSO, 24 hr) / Silvestrol (6.25 nM, 24 hr) / Rocaglamide A (6.25 nM, 24 hr) / Zotatifin (12.5 nM, 24 hr)

C

DMSO / Silvestrol (12.5 nM)

Relative total cell number

siRNA: NS RHOA / NS RHOA

D U87MG

GEF-H1
CD98hc
MYC
eIF4A2
CYPB

0 1 2 4 8 12 24 48

Silvestrol (6.25 nM) duration (hr)

Log₂ mRNA translation efficiency

eIF4A2 * GEF-H1 * CD98hc

Translation efficiency = Polysome:free/monosome ratio

■ DMSO ■ Silvestrol (6.25 nM, 8 hr)

E

Silvestrol (6.25 nM), 8 hr

Free | Mono | Oligo | Poly

Absorbance at 254 nm

40S 60S 80S

Ribosome density

Vehicle (DMSO), 8 hr

Free | Mono | Oligo | Poly

40S 60S 80S

Ribosome density

F U87MG (cell viability)

Relative log₂ cell viability (normalized to vehicle control)

0.2 0.0 -0.2 -0.4 -0.6

Concentration (nM, 24 hr): 0 0.78 1.56 3.13 6.25 12.5 25 50 100

— Silvestrol
— Zotatifin

Figure S3.

Figure S3. Rocaglate-inducible GEF-H1 regulates JNK signaling via RHOA in malignant cells, related to Figure 2. (**A**) Representative immunoblots of BJAB and HeLa treated with silvestrol (6.25 nM) or vehicle (DMSO) for 24 hr. Densitometry values are normalized to loading control. (**B**) Representative immunoblots of NIH/3T3 mouse embryonic fibroblasts treated with silvestrol (6.25 nM), rocaglamide A (6.25 nM), zotatifin (12.5 nM) or vehicle (DMSO) for 24 hr. (**C**) Relative total cell number of U87MG treated with indicated siRNA pools (100 nM final concentration) for 72 hr, followed by treatment with silvestrol (12.5 nM) or vehicle (DMSO) for 24 hr. Data represent mean ± SEM (error bars) of three independent experiments. * indicates $p < 0.05$ compared to NS (non-silencing) siRNA control. (**D**) Representative immunoblots of U87MG treated with silvestrol (indicated concentrations) for indicated durations. (**E**) Ribosome density profiles (left panel) and mRNA translation efficiency (abundance ratio of polysome-associated mRNA to ribosome-free and monosome-associated mRNA) (right panel) of U87MG treated with silvestrol (6.25 nM) or vehicle (DMSO) for 8 hr. Data represent mean ± SEM (error bars) of five independent experiments. * denotes $p < 0.05$ compared to vehicle (DMSO) treatment. of U87MG treated with silvestrol (6.25 nM) or vehicle (DMSO) for 8 hr. (**F**) Relative cell viability based on ATP levels in U87MG treated with indicated concentrations of silvestrol or zotatifin for 24 hr (left panel) or 48 hr (right panel). Data represent mean ± SEM (error bars) of four independent cell populations. * and ** indicate $p < 0.05$ and $p < 0.01$, respectively compared to vehicle-treated condition.
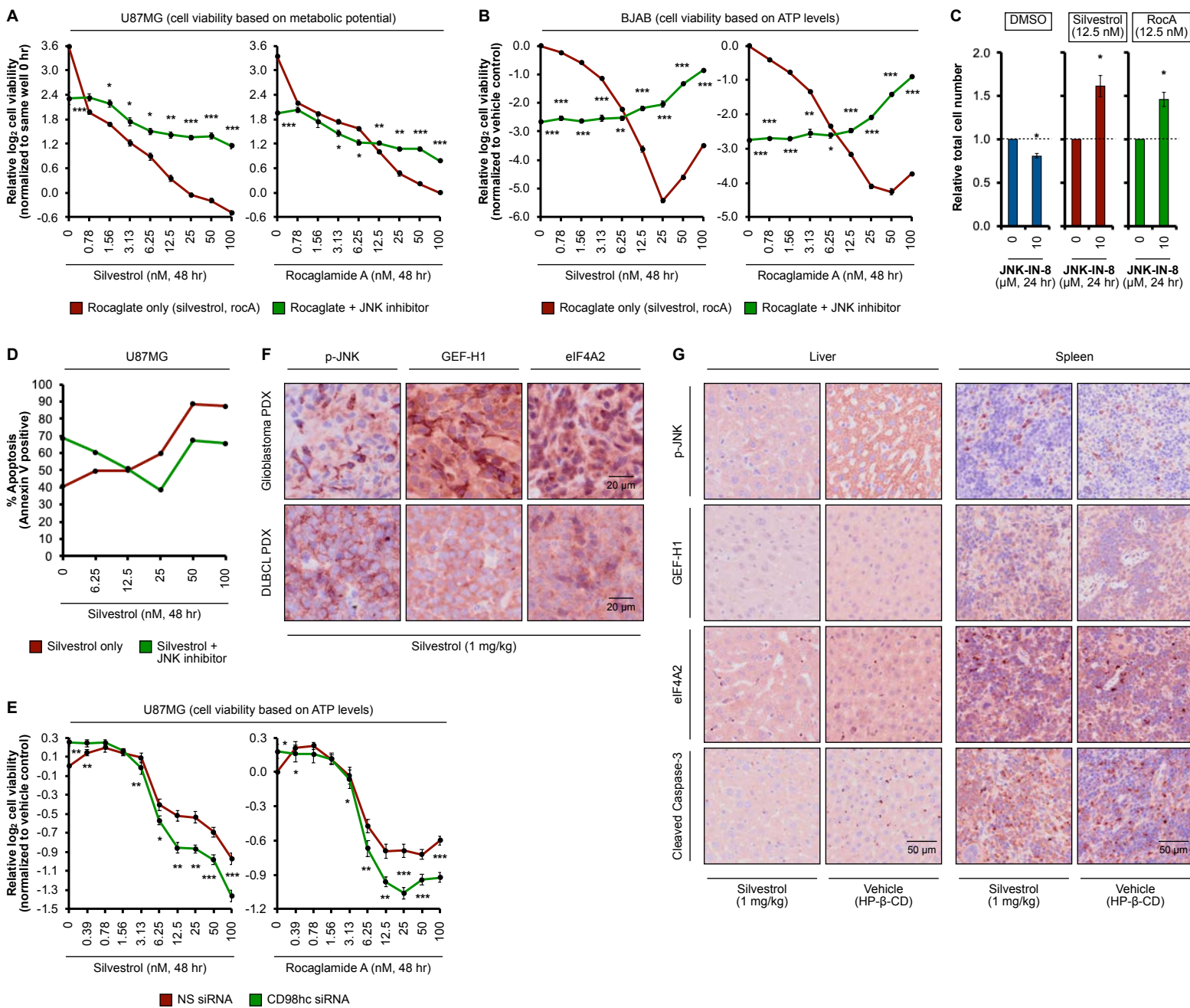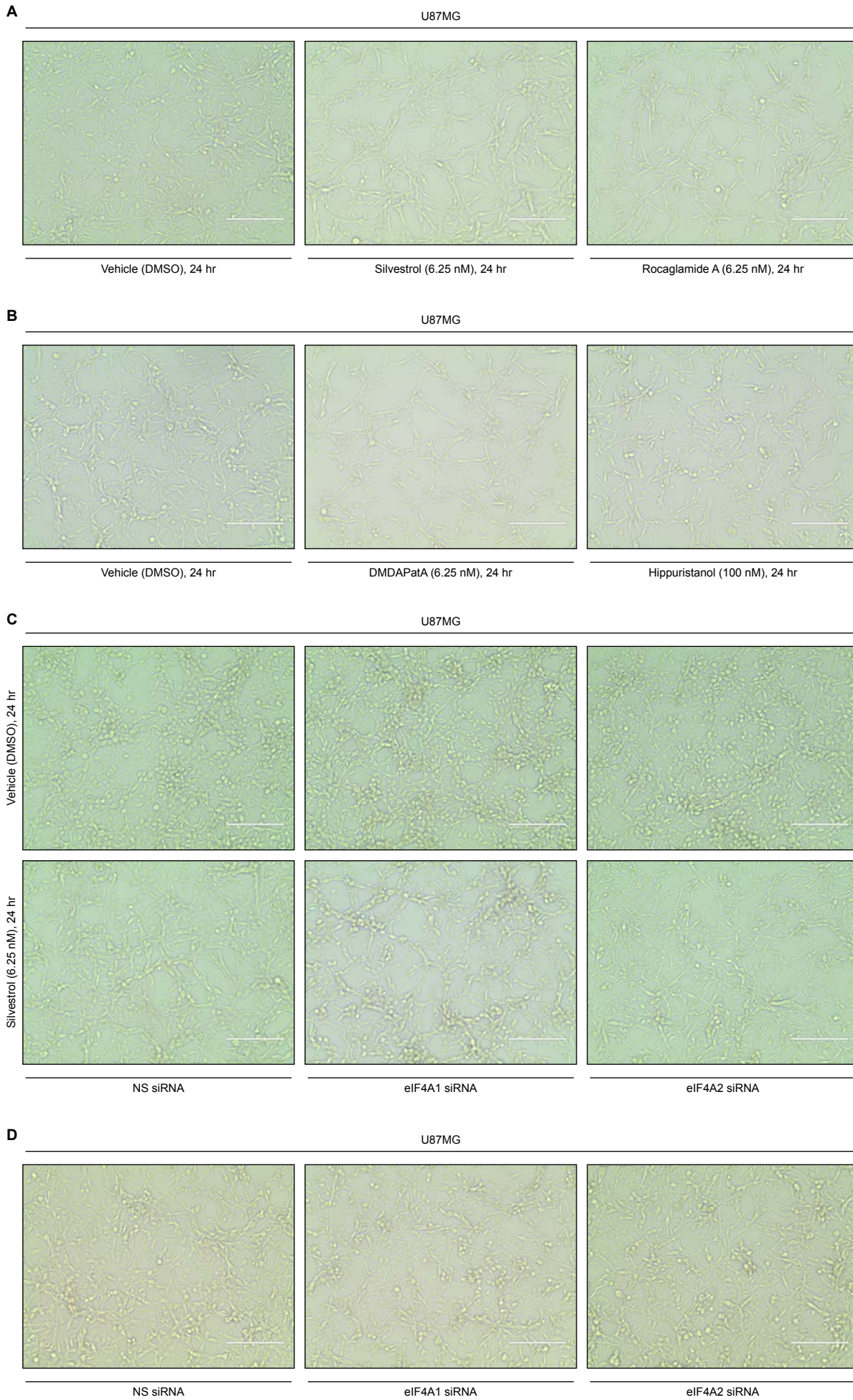
Figure S4.

Figure S4. Rocaglate-inducible JNK phosphorylation mediates cellular toxicity signaling, related to Figure 3. (**A**) Relative cell viability based on cellular metabolic potential in U87MG treated with indicated concentrations of silvestrol (left panel) or rocaglamide A (right panel) with and without JNK inhibitor JNK-IN-8 (10 μM) for 48 hr. Data represent mean ± SEM (error bars) of four independent cell populations. *, **, and *** indicate $p < 0.05$, $p < 0.01$, and $p < 0.001$, respectively, compared to corresponding rocaglate only condition. (**B**) Relative cell viability based on ATP levels in BJAB treated with indicated concentrations of silvestrol and rocaglamide A, with and without JNK inhibitor JNK-IN-8 (10 μM) for 48 hr. Data represent mean ± SEM (error bars) of four independent cell populations. *, **, and *** indicate $p < 0.05$, $p < 0.01$, and $p < 0.001$, respectively, compared to corresponding rocaglate only condition. (**C**) Relative total cell number of U87MG treated with silvestrol (12.5 nM), rocaglamide A (rocA, 12.5 nM), or vehicle (DMSO), with and without JNK inhibitor JNK-IN-8 (10 μM) for 24 hr. Data represent mean ± SEM (error bars) of three independent experiments. * denotes statistical significance compared to vehicle (DMSO). (**D**) Percent apoptosis in U87MG treated with indicated concentrations of silvestrol or vehicle (DMSO) with and without JNK inhibitor JNK-IN-8 (10 μM) for 48 hr. Representative experiment shown. Three independent experiments were performed. (**E**) Relative cell viability of U87MG treated with indicated siRNA pools (50 nM final concentration) for 48 hr, followed by indicated concentrations of silvestrol (left panel) or rocaglamide A (right panel) for 48 hr. Data represent mean ± SEM (error bars) of four independent cell populations. *, **, and *** indicate $p < 0.05$, $p < 0.01$, and $p < 0.001$, respectively, compared to corresponding NS siRNA control. Representative immunohistochemistry images of (**F**) glioblastoma and DLBCL PDX tumors (scale bar represents 20 μm) , (**G**) liver (left panel) and spleen (right panel) of mice treated with silvestrol (1 mg/kg) or vehicle (2-hydroxypropyl-β-cyclodextrin) (daily intraperitoneal injection for three days) (scale bar represents 50 μm).

A

U87MG

Vehicle (DMSO), 24 hr

Silvestrol (6.25 nM), 24 hr

Rocaglamide A (6.25 nM), 24 hr

B

U87MG

Vehicle (DMSO), 24 hr

DMDAPatA (6.25 nM), 24 hr

Hippuristanol (100 nM), 24 hr

C

U87MG

Vehicle (DMSO), 24 hr

Silvestrol (6.25 nM), 24 hr

NS siRNA

eIF4A1 siRNA

eIF4A2 siRNA

D

U87MG

NS siRNA

eIF4A1 siRNA

eIF4A2 siRNA

Figure S5.

Figure S5. Mechanisms of rocaglate-dependent protein induction, related to Figure 4. (**A**) Representative bright field images of U87MG treated with silvestrol (6.25 nM), rocaglamide A (6.25 nM), or vehicle (DMSO) for 24 hr. (**B**) Representative bright field images of U87MG treated with DMDAPatA (6.25 nM), hippuristanol (100 nM), or vehicle (DMSO) for 24 hr. Scale bars in (a) to (d) represent 200 μm. (**C**) Representative bright field images of U87MG treated with indicated siRNA pools (50 nM final concentration) for 48 hr, followed by silvestrol treatment (6.25 nM) or vehicle (DMSO) for 24 hr. (**D**) Representative bright field images of U87MG treated with indicated siRNA pools (50 nM final concentration) for 48 hr. NS: non-silencing.
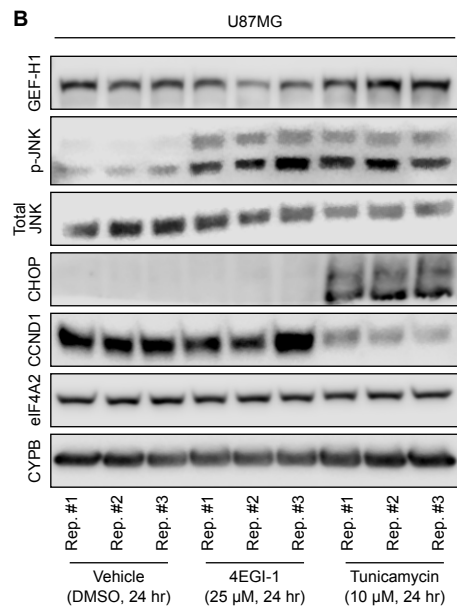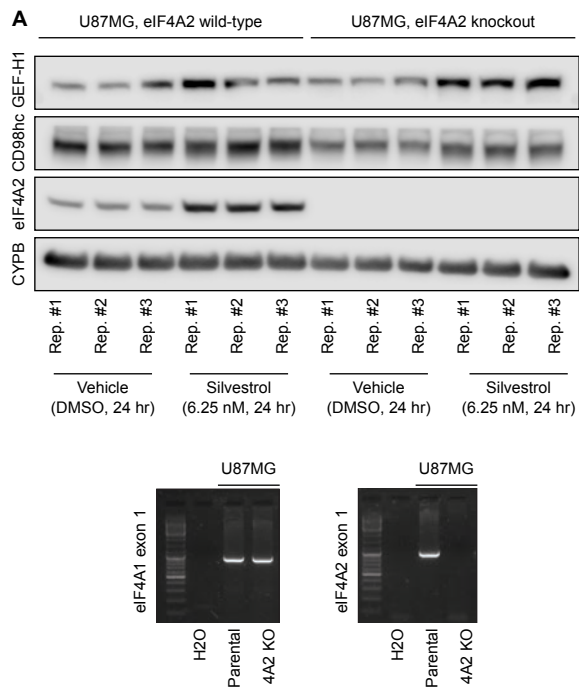
A

U87MG, eIF4A2 wild-type   U87MG, eIF4A2 knockout

GEF-H1

CD98hc

eIF4A2

CYPB

Rep. #1   Rep. #2   Rep. #3   Rep. #1   Rep. #2   Rep. #3   Rep. #1   Rep. #2   Rep. #3   Rep. #1   Rep. #2   Rep. #3

Vehicle (DMSO, 24 hr)   Silvestrol (6.25 nM, 24 hr)   Vehicle (DMSO, 24 hr)   Silvestrol (6.25 nM, 24 hr)

eIF4A1 exon 1

U87MG

H2O   Parental   4A2 KO

eIF4A2 exon 1

U87MG

H2O   Parental   4A2 KO

B

U87MG

GEF-H1

p-JNK

Total JNK

CHOP

CCND1

eIF4A2

CYPB

Rep. #1   Rep. #2   Rep. #3   Rep. #1   Rep. #2   Rep. #3   Rep. #1   Rep. #2   Rep. #3

Vehicle (DMSO, 24 hr)   4EGI-1 (25 µM, 24 hr)   Tunicamycin (10 µM, 24 hr)

Figure S6.

Figure S6. Mechanisms of rocaglate-dependent protein induction, related to Figure 4
(**A**) Representative immunoblots of U87MG eIF4A2 wild-type or eIF4A2 knockout cells treated with silvestrol (6.25 nM) or vehicle (DMSO) for 24 hr (top panel). Genomic DNA PCR analysis of exon 1 of eIF4A1 and eIF4A2 in U87MG parental and 4A2 KO cells (bottom panel). (**B**) Representative immunoblots of U87MG treated with 4EGI-1 (25 μM), tunicamycin (10 μM) or vehicle (DMSO) for 24 hr.
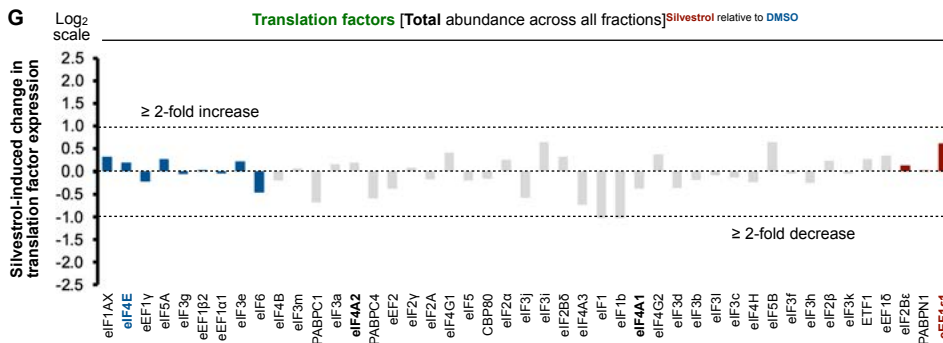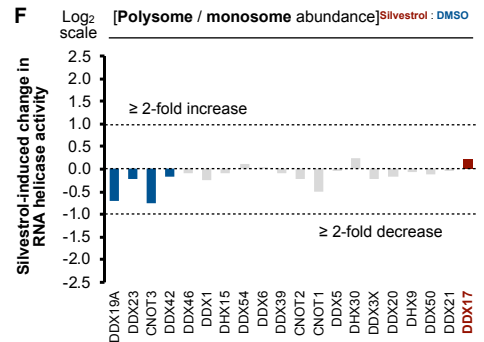
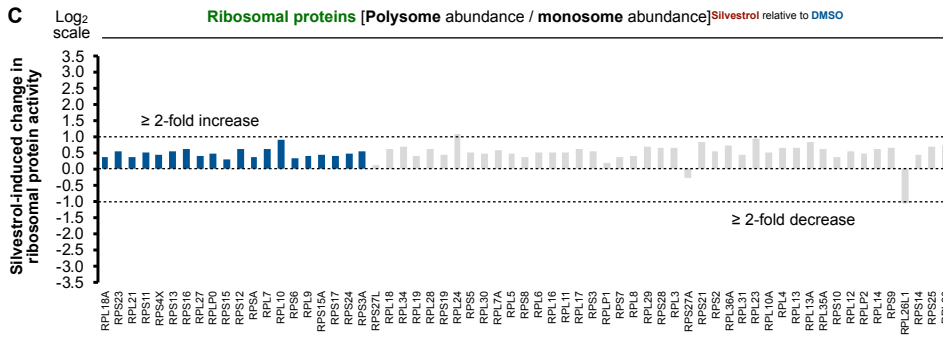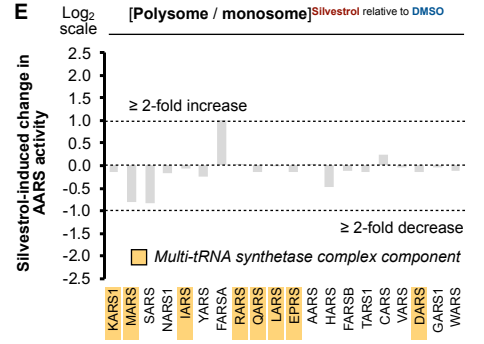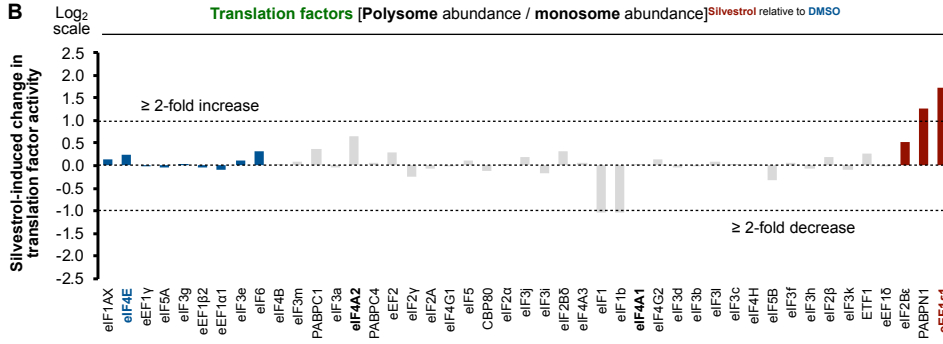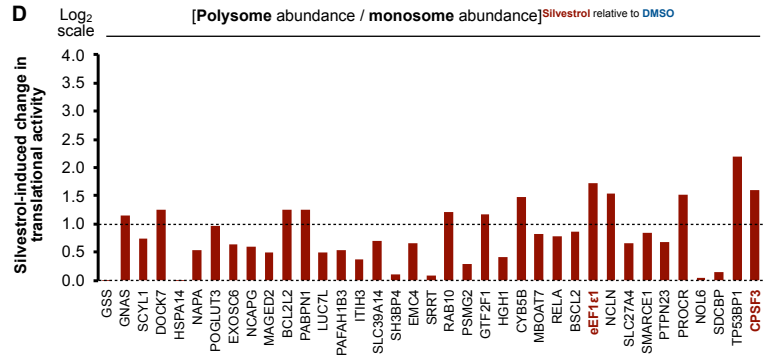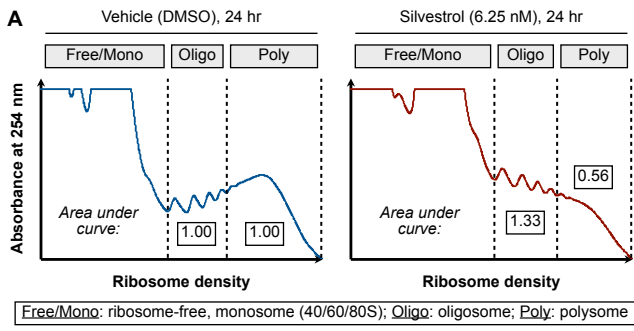**Figure S7.**

Figure S7. System-wide survey of rocaglate-dependent changes in the translation machinery, related to Figure 5. (**A**) Ribosome density profiles of U87MG treated with vehicle (DMSO) or silvestrol (6.25 nM) for 24 hr. Samples were loaded based on equal total RNA content. 2x more total RNA was loaded compared to Figure 4A. MATRIX analysis of silvestrol-induced changes in translational activity (i.e. ratio of protein abundance in polysome versus monosome (40/60/80S) fraction) for (**B**) canonical translation factors, (**C**) ribosomal proteins, (**D**) most highly induced proteins (≥ 3x activity enrichment), (**E**) aminoacyl-tRNA synthetases (AARSs), and (**F**) DEAD/DEAH RNA helicases. (**G**) Total sum of protein abundances across all MATRIX fractions in silvestrol- versus vehicle-treated samples. Proteins (x-axis) are arranged in the same order as panels B-F of Figure 5. Blue and red indicate silvestrol-repressed and silvestrol-activated translational assets (≥ 2x difference in activity), respectively, based on [polysome/free] protein abundance ratios as shown in Figure 5.
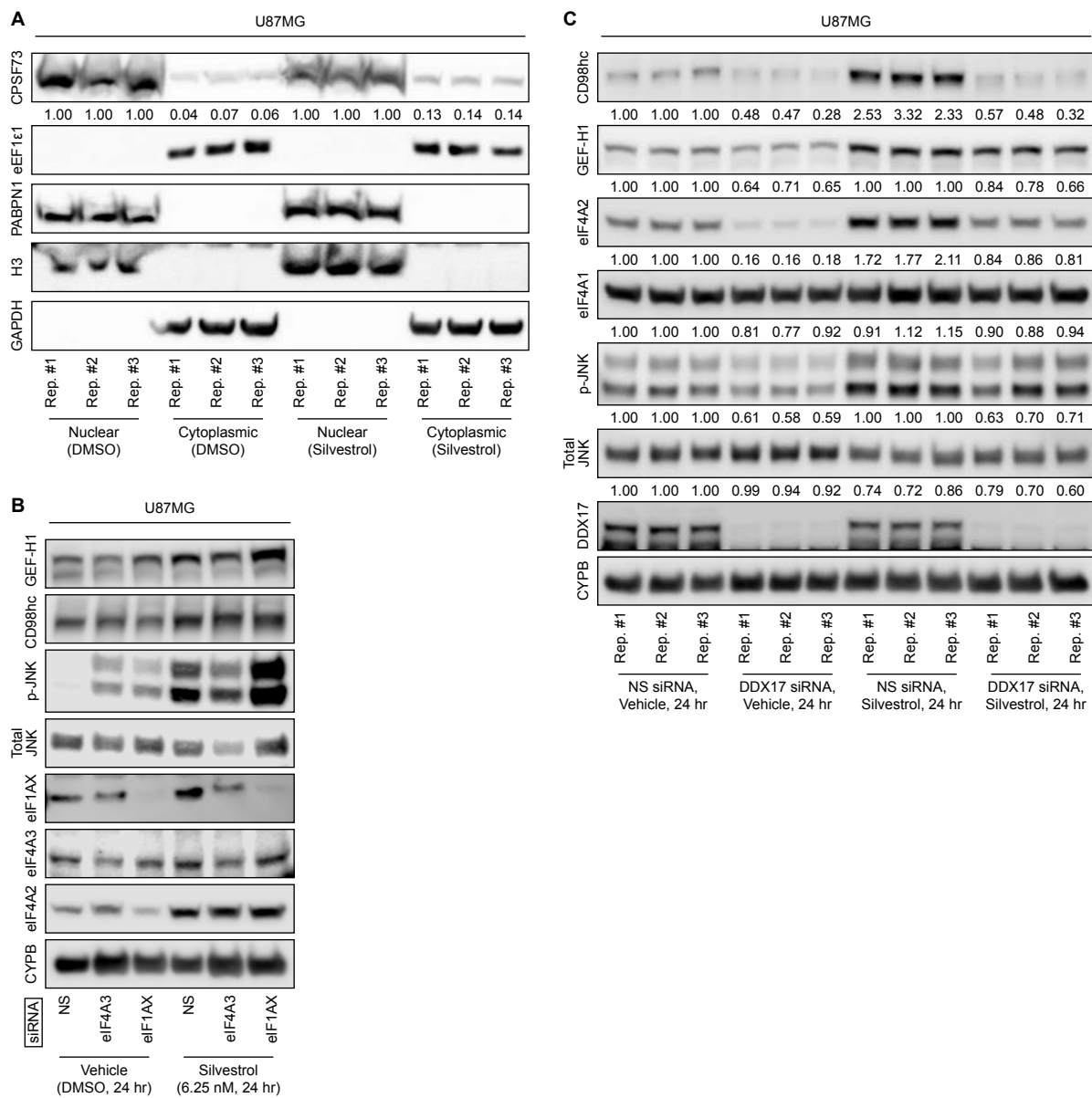
A

U87MG

CPSF73

1.00 1.00 1.00 0.04 0.07 0.06 1.00 1.00 1.00 0.13 0.14 0.14

eEF1ε1

PABPN1

H3

GAPDH

Rep. #1 Rep. #2 Rep. #3 | Rep. #1 Rep. #2 Rep. #3 | Rep. #1 Rep. #2 Rep. #3 | Rep. #1 Rep. #2 Rep. #3

Nuclear (DMSO) | Cytoplasmic (DMSO) | Nuclear (Silvestrol) | Cytoplasmic (Silvestrol)

B

U87MG

GEF-H1

CD98hc

p-JNK

Total JNK

eIF1AX

eIF4A3

eIF4A2

CYPB

siRNA: NS eIF4A3 eIF1AX NS eIF4A3 eIF1AX

Vehicle (DMSO, 24 hr) | Silvestrol (6.25 nM, 24 hr)

C

U87MG

CD98hc

1.00 1.00 1.00 0.48 0.47 0.28 2.53 3.32 2.33 0.57 0.48 0.32

GEF-H1

1.00 1.00 1.00 0.64 0.71 0.65 1.00 1.00 1.00 0.84 0.78 0.66

eIF4A2

1.00 1.00 1.00 0.16 0.16 0.18 1.72 1.77 2.11 0.84 0.86 0.81

eIF4A1

1.00 1.00 1.00 0.81 0.77 0.92 0.91 1.12 1.15 0.90 0.88 0.94

p-JNK

1.00 1.00 1.00 0.61 0.58 0.59 1.00 1.00 1.00 0.63 0.70 0.71

Total JNK

1.00 1.00 1.00 0.99 0.94 0.92 0.74 0.72 0.86 0.79 0.70 0.60

DDX17

CYPB

Rep. #1 Rep. #2 Rep. #3 | Rep. #1 Rep. #2 Rep. #3 | Rep. #1 Rep. #2 Rep. #3 | Rep. #1 Rep. #2 Rep. #3

NS siRNA, Vehicle, 24 hr | DDX17 siRNA, Vehicle, 24 hr | NS siRNA, Silvestrol, 24 hr | DDX17 siRNA, Silvestrol, 24 hr

Figure S8.

Figure S8. Increased eEF1ε1 activity enables rocaglate-driven protein synthesis, related to Figure 6. (**A**) Representative immunoblots of nuclear and cytoplasmic fractions from U87MG treated with silvestrol (6.25 nM) or vehicle (DMSO) for 24 hr. Histone H3 and GAPDH are shown as nuclear and cytoplasmic controls, respectively. (**B**) Representative immunoblots of U87MG treated with silvestrol (6.25 nM) or vehicle (DMSO) for 24 hr. (**C**) Representative immunoblots of U87MG treated with indicated siRNA pools for 48 hr, followed by treatment with silvestrol (6.25 nM) or vehicle (DMSO) for 24 hr. Densitometry values in are normalized to loading control.